

Three-dimensional quantum anomalous Hall effect in Weyl semimetals

Zhi-Qiang Zhang^{1,2,8}, Yu-Hang Li^{3,4,8}, Ming Lu⁵, Hongfang Liu², Hailong Li^{1,6}, Hua Jiang^{1,✉}, and X. C. Xie^{1,6,7}

¹*Interdisciplinary Center for Theoretical Physics and Information Sciences (ICTPIS), Fudan University, Shanghai 200433, China*

²*School of Physical Science and Technology, Soochow University, Suzhou 215006, China*

³*School of Physics, Nankai University, Tianjin 300071, China*

⁴*State Key Laboratory of the Surface Physics and Department of Physics, Fudan University, 200433, Shanghai, China*

⁵*Beijing Academy of Quantum Information Sciences, Beijing 100193, China*

⁶*International Center for Quantum Materials, School of Physics, Peking University, Beijing 100871, China*

⁷*Hefei National Laboratory, Hefei 230088, China*

The quantum anomalous Hall effect (QAHE) is a quantum phenomenon in which a two-dimensional system exhibits a quantized Hall resistance h/e^2 in the absence of magnetic field, where h is the Planck constant and e is the electron charge. In this work, we extend this novel phase to three dimensions and thus propose a three-dimensional QAHE exhibiting richer and more versatile transport behaviors. We first confirm this three-dimensional QAHE through the quantized Chern number, then establish its bulk-boundary correspondence, and finally reaffirm it via the distinctive transport properties. Remarkably, we find that the three-dimensional QAHE hosts two chiral surface states along one spatial direction while a pair of chiral hinge states along another direction, and the location of the hinge states depends sensitively on the Fermi energy. These two types of boundary states are further connected through a perpendicular chiral surface states, whose chirality is also Fermi energy dependent. Consequently, depending on the transport direction, its Hall resistance can quantize to 0 , h/e^2 , or $\pm h/e^2$ when the Fermi energy is tuned across the charge neutral point. This three-dimensional QAHE not only fill the gap in the Hall effect family but also holds significant potentials in device applications such as in-memory computing.

The discovery of the quantum Hall effect in the presence of a relatively strong magnetic field has profoundly inspired the study of topological phase of matter¹⁻¹⁶, which not only deepens our understanding of condensed materials beyond the scope of symmetry breaking but also holds significant promises in device application with low or even zero energy dissipation. In principle, since the role of magnetic field can be completely replaced by spontaneous magnetic ordering, quantum Hall effect^{6,14,15} and its anomalous counterpart, termed quantum anomalous Hall effect^{4,17,18}, typically appear as complimentary pair. These two prominent states can be unifyingly understood within the framework of the Thouless-Kohmoto-Nightingale-Nijs (TKNN) theory^{19,20}, which connects them and their essential properties, such as the quantized Hall resistance $R_h = h/e^2$, with intuitive band topology characterized by the first Chern number \mathcal{C} through the bulk-boundary

⁸ These authors contributed equally to this work: Zhi-Qiang Zhang and Yu-Hang Li.

✉e-mail:jianghuaphy@fudan.edu.cn

correspondence^{21,22}. While the quantum Hall effect was recently extended to three-dimensional case²³⁻²⁸, leading to the successful observation of the three-dimensional quantum Hall effect with strongly enhanced tunability²⁹⁻³³, its anomalous counterpart in three dimensions still stands as a gap in the Hall effect family.

In this work, we demonstrate the realization of the three-dimensional quantum anomalous Hall effect (3D QAHE) in a cubic Weyl semimetal (WSM)³⁴⁻⁴⁰ and thus fill this outstanding gap. In a WSM harboring two pairs of Weyl nodes, we find that a Rashba spin-orbit coupling can open a trivial band gap with vanishing topological invariant in the bulk and simultaneously, an inverted band gap on opposite top and bottom surfaces. These two gaped surfaces both possess a half-quantized Chern number, therefore realizing a 3D QAHE characterized by $\mathcal{C} = 0.5 + 0.5$. Unlike the two-dimensional case^{4,17}, this 3D QAHE hosts a pair of extended chiral surface states along one direction while two chiral hinge states along another vertical direction. Interestingly, the location of these two hinge states is intimately bound to the Fermi energy, which can move from one pair of diagonal hinges to the other pair when the Fermi energy is adjusted across the charge neutral point. Besides, the hinge states and the surface states are further connected by a pair of Fermi energy-dependent chiral surface states perpendicular to both. These peculiar boundary states in turn lead to a distinctive transport behavior, where the Hall resistance can be 0 , h/e^2 , or $\pm h/e^2$ along different directions when adjusting the Fermi energy across the charge neutral point. Furthermore, our transport simulations also find fractionally quantized Hall resistances that originates from the spatial confinement, indicating an emergent topology from the finite-size effect. Because the sign of quantized Hall resistance is directly bound to the Fermi energy, which can be finely manipulated through a top gate, this 3D QAHE thus holds significant promises in device applications such as in-memory computing. Possible candidate materials for realizing this 3D QAHE are also discussed.

Results

Model for the 3D QAHE

We begin with the following Hamiltonian defined on a cubic lattice

$$H = \mathcal{H}_w \sigma_z + \sum_n [i t_s (\sigma_x c_n^\dagger c_{n+\delta_x} + \sigma_y c_n^\dagger c_{n+\delta_y}) + \text{h.c.}], \quad (1)$$

where $\mathcal{H}_w = \sum_n \mathcal{T}_0 c_n^\dagger c_n + \sum_{\alpha=x,y,z} \mathcal{T}_\alpha c_n^\dagger c_{n+\delta_\alpha} + \text{h.c.}$ is a typical Hamiltonian for a WSM with $\mathcal{T}_0 = -4m\tau_z - \lambda$, $\mathcal{T}_x = m_x\tau_z$, $\mathcal{T}_y = m\tau_z - iA\tau_y$ and $\mathcal{T}_z = m\tau_z - iA\tau_x$ ^{25,30}. Here, $\sigma_{x,y,z}$ ($\tau_{x,y,z}$) are Pauli matrices acting on spin (pseudospin) spaces, c_n^\dagger (c_n) is the electron creation (annihilation) operator at site n , $\delta_{\alpha=x,y,z}$ is the lattice constant along α direction, which is set to be the length unit, and h.c. refers to the Hermitian conjugate. As shown in Figs. 1a and b, the first term in Eq. (1) describes a WSM harboring two pairs of Weyl nodes located at $\mathbf{k}_w^\pm = (\pm\pi/2, 0, 0)$ with an energy split $E_\pm = \pm\lambda$. In this case, the Fermi arc band at the charge neutral point forms a closed manifold as indicated by the Green lines in Figs. 1a-b, which thus enable us to construct the band topology. The second term is a conventional Rashba spin-orbit coupling with t_s being its strength. Note that the system described by Eq. (1) breaks the time-reversal symmetry (\mathcal{T}) explicitly while preserves the space inversion symmetry (\mathcal{I}) that can be defined as $\mathcal{I} = I_2 \otimes \sigma_z$. Without loss of generality, the system parameters are hereafter fixed as $m = m_x = t$ and $A = \lambda = t_s = 0.5t$ with

t the energy unit.

Band properties and topological invariants

Imposing periodic boundary conditions along all three spatial directions renders us to calculate the bulk band spectrum in the momentum space (Methods), which is displayed in Fig. 1c along a closed loop connecting all highly symmetric points within the first Brillouin zone (1st BZ). It is evident that the bulk bands are largely gaped with a gap size of $\Delta \approx 2t$ highlighted by the gray shadow, which excludes the contribution to the topology of the system from these bulk bands. Besides, the bulk topology in three dimensions analogous to 3D QAHE, such as a second order topological insulator, can generally be revealed through the octupole moment Q_{xyz} defined as^{41,42}

$$Q_{xyz} = \sum_{E_n < 0} \frac{1}{(2\pi)^3} \int_{\text{1st BZ}} d^3\mathbf{k} \text{Tr}(A_x^n A_y^n A_z^n), \quad (2)$$

where $A_{\alpha=x,y,z}^n = i\langle \psi_{n\mathbf{k}} | \partial_{k_\alpha} \psi_{n\mathbf{k}} \rangle$ is the Berry connection of n -th Bloch band with E_n the eigenenergy and $|\psi_{n\mathbf{k}}\rangle$ the eigenwavefunction. As labeled in Fig. 1c, the octupole moment of the system turns out to be identically zero, which contradicts a high order topological phase characterized by $Q_{xyz} = 1$ ⁴¹⁻⁴⁴, which therefore removes the possibility of bulk topology.

To explore the surface bands, we then consider a slab geometry terminated along one (x , y , or z) of three spatial directions and show the band dispersions in Figs. 1d-f (Methods). The average position $\langle \alpha/L_\alpha \rangle$ ($\alpha = x, y, z$) is also provided in each figure, which features the location of the wavefunction with respect to the slab⁴⁵. On the x - y plane, the surface band spectrum in Fig. 1d is obviously gaped, whose gap minima, coincident with the surface Dirac cone without Rashba spin-orbit coupling (Fig. 1a), are shifted oppositely along k_y . Moreover, the surface bands with negative k_y are overall confined to the bottom surface at $\langle z/L_z \rangle = -0.5$ (blue region) while those with positive k_y are confined to the opposite top surface at $\langle z/L_z \rangle = 0.5$ (red region), manifesting a momentum-surface locking guaranteed by the space inversion symmetry. Notably, when the Fermi energy E_f lies inside this gap, each surface band possesses a half-quantized Chern number, leading to a jointly quantized Chern number $\mathcal{C}_{xy} = 1$. In contrast, despite that the surface band on the z - x plane also manifests a momentum-surface locking with negative (positive) k_z bands confined to the left (right) surface at $\langle y/L_y \rangle = -0.5$ ($\langle y/L_y \rangle = 0.5$), the band spectrum on this plane is gapless with a vanishing Chern number $\mathcal{C}_{zx} = 0$ as shown in Fig. 1e. On the y - z plane, the band spectrum is also gapless with the Dirac cone located exactly at $k_y = k_z = 0$, which is nevertheless doubly degenerated because of the inherent space inversion symmetry. One of these degenerated bands is confined to the front surface at $\langle x/L_x \rangle = 0.5$ while the other is confined to the opposite back surface at $\langle x/L_x \rangle = -0.5$. Therefore, this quantized Chern number $\mathcal{C}_{xy} = 1$ characterizes a 3D QAHE that exists only on the surface of a three-dimensional WSM. We also ascertain that the non-zero Berry curvature originates completely from the surface bands (Supplementary Note 2), further excluding the contribution from the bulk.

Bulk-boundary correspondence in 3D QAHE

In view of the bulk-boundary correspondence^{21,22}, the quantized Chern number along z direction equivalently indicates a low dimension boundary excitation if the system is terminated along x

or (and) y directions. To unveil these boundary states, we consider a one dimensional nanowire with open boundary conditions along y and z directions, and calculate its band spectrum as a function of k_x . The results plotted in the left panel of Fig. 2a confirm the existence of two gapless boundary states with opposite group velocities (red and blue lines). In addition, the wavefunction distributions across the lateral y - z plane in the right panel for two representative Fermi energies (black dashed lines) show that these two boundary states extend universally along z direction, whose chiralities do not depend on the Fermi energy E_f . We next turn to a nanowire with open boundary conditions along x and z directions. The band spectrum in Fig. 2b, analogous to that in the former case, also hosts two chiral boundary states represented by red and blue lines. However, these two boundary states are mostly confined to two diagonal hinges of the cross section on the z - x plane, and their locations switch from one pair of diagonal hinges to the other pair when the Fermi energy varies across the charge neutral point at $E = 0$, showcasing a pair of energy-dependent chiral hinge states.

Although all boundary states are triggered by the Chern number difference among nontrivial top (or bottom) surface and neighboring lateral surfaces, the distinct behaviors of these two types of boundary states originate from the anisotropic band structures along different directions. Specifically, the Dirac cones on the left (right) surface and the top (bottom) surface coincide exactly at the same k_x as shown in Fig. 2c (top panel), so that the side surface is metallic, allowing the boundary state to evolve intactly across the entire left (right) surface (bottom panel). On the contrary, as shown in Fig. 2d, the top and bottom bands are shifted oppositely along k_y whereas the front and back bands remain at $k_y = 0$ (top panel). In this case, the boundary state, for example the one marked by the red dot, lies at the gap of the front and back surface bands unless near the charge neutral point, which thus decays exponentially into these two surfaces (bottom panel), leading to a pair of chiral hinge states. Furthermore, due to the momentum-surface locking (Fig. 1d), the state with $k_y < 0$ ($k_y > 0$) is confined to the top (bottom) surface at $\langle z/L_z \rangle = 0.5$ ($\langle z/L_z \rangle = -0.5$). When adjusting the Fermi energy E_f across the charge neutral point at $E = 0$, the group velocities of both states flip, which thus move to the other pair of diagonal hinges.

While the boundary states inherent to the quantized Chern number $\mathcal{C}_{xy} = 1$ have been established, there still exists an unresolved puzzle about the connection between these two different types of boundary states, as their chiralities forbid bending or opposite electron propagating on one surface. To ensure a smooth connection between them, additional vertical chiral states are naturally required, which are anticipated to be also Fermi energy dependent. To uncover hidden boundary states in the 3D QAHE, we further consider a nanowire with open boundary conditions along x and y directions. Figure 2e displays the band spectrum as a function of k_z and also the average position $\langle y/L_y \rangle$ for four low energy bands close to the charge neutral point $E = 0$. Despite of the mixing near $k_z = 0$, the wavefunctions of the central two surface bands (colorful lines ± 1) are mostly confined to left ($\langle y/L_y \rangle = -0.5$ when $k_z < 0$) or right ($\langle y/L_y \rangle = 0.5$ when $k_z > 0$) surfaces with opposite group velocities, which are protected by a large band gap highlighted by the gray shadows. This thus confirms the existence of two vertical chiral surface states that can be ascribed to the coupling among neighboring lateral surface bands.

As illustrated in Fig. 2f, in the absence of coupling near the vertical hinges, the gapless Dirac cones on the left and right surfaces are shifted oppositely along k_z while those on the front and back surfaces remain at $k_z = 0$. Incorporating the coupling through the common hinge between two neighboring lateral surfaces immediately opens band gaps near the cross regions highlighted by the magenta circles, which simultaneously, eliminates two oppositely propagating surface states denoted by the thin arrows. During this process, only two chiral states survive separately on left and right surfaces. When tuning the Fermi energy across the charge neutral point, the chiralities of these two surface states flip due to the reversal of the group velocities, so they are also Fermi energy dependent. Consequently, this 3D QAHE altogether hosts two chiral surface states along x direction, a pair of Fermi energy dependent chiral hinge states along y direction, and a pair of chiral surface states along z direction that are also Fermi energy dependent. This bulk-boundary correspondence, which is schematically summarized in Fig. 2g, is instructive to understand the transport properties of the 3DQAHE.

Transport properties

The crucial fingerprint of the QAHE is the quantized Hall resistance accompanied by a vanishing longitudinal one^{4,10,18}, which can be confirmed by the transport measurement in a Hall bar setup with two longitudinal and four transverse leads. In experiment, the Hall and longitudinal resistances can be extracted reliably from the voltages detected on each transverse leads under a longitudinal current. To explore the transport properties of the 3D QAHE, we consider a same Hall bar structure and calculate its Hall and longitudinal resistances by using the Landauer-Büttiker theory⁴⁶. In three dimensions, the current can be applied arbitrarily along all three spatial directions, and in each case, the transverse leads can be attached distinctly along two vertical directions both perpendicular to applied current direction, so there are altogether six geometry allowed Hall bar configurations as depicted in Figs. 3a-c. For clarity, we denote the Hall and longitudinal resistances in forms of $R_{\beta\gamma}^\alpha$ and $R_{\beta\beta}^\alpha$, respectively, with $\alpha, \beta, \gamma = x, y, z$, where β is the current applied direction, γ is the transverse direction while α is the direction perpendicular to the Hall bar plane.

Since the transport in each Hall bar configuration is entirely dominated by involved boundary states, the transport behavior can be analyzed qualitatively from the edge picture. As shown in Fig. 3a, when the current is applied along x direction, only the chiral surface states contribute to the transport. If the transverse leads are attached along y direction (top panel), the Hall resistance R_{xy}^z is anticipated to be quantized to h/e^2 while the longitudinal resistance R_{xx}^z is zero when E_f lies inside the inverted band gap. However, if the transverse leads are attached along z direction (bottom panel), since the x - y surface are largely gaped, the longitudinal resistance R_{xx}^y is generally large but unquantized while the Hall resistance R_{xz}^y is vanishing because of the absence of transport channel. When the applied current becomes parallel to y direction, the transport in this case is dominated by the Fermi energy dependent chiral hinge states as illustrated in Fig. 3b. If the transverse leads are attached along x direction (top panel), although the hinge states move from one pair of diagonal hinges on the cross section to the other pair when E_f varies across the charge neutral point at $E = 0$, the Hall resistance R_{yx}^z remains quantized to h/e^2 with a vanishing longitudinal resistance R_{yy}^z since the chirality persists. On the contrary, if the transverse leads are attached along z direction (bottom panel), because the chirality of the chiral hinge states flips, R_{yz}^x switches between $\pm h/e^2$ during the manipulation of E_f . Finally, when the current is applied

along z direction (Fig. 3c), the transport is dominated by the Fermi energy dependent chiral surface states, whose chirality also flips when adjusting the Fermi energy. Therefore, R_{zy}^x switches between $\pm h/e^2$ with $R_{zz}^x = 0$ (top panel) when tuning E_f across the charge neutral point whereas R_{zx}^y is by contrast zero with a large but unquantized R_{zz}^y (bottom panel). As shown in Figs. 3d-f, the numerical results obtained by using the Landauer-Büttiker theory (Supplementary Note 3) agree remarkably well with above analysis based on involved boundary states. Meanwhile, the quantized Hall resistance and the vanishing longitudinal resistance are robust against relatively strong Anderson disorders⁴⁷, reaffirming the topological nature of this 3D QAHE.

Fractional-quantized Hall resistance and in-memory computing

In addition to the band gap highlighted by the gray shadows, the spectrum in Fig. 2e has another similar gaps highlighted by the magenta shadows that separate two additional chiral surface bands (colorful lines ± 2) from the high energy bands (gray lines). When the Fermi energy lies inside these gaps, for example at $E_f = 0.33t$, two chiral surface channels (surface state ± 1 and ± 2) are altogether involved in the transport, so that the Hall resistance should identically quantize to $h/2e^2$. Figure 4a shows R_{zy}^x and R_{zz}^x as functions of E_f on a 3D QAHE with size $L_y = L_z = 8$. When E_f varies across the charge neutral point, R_{zy}^x switches from $-h/e^2$ to h/e^2 , in agreement with that in Figs. 3c and f. As E_f further deviates from the charge neutral point, R_{zy}^x consecutively quantizes to $\pm h/2e^2$, $\pm h/3e^2$ and $\pm h/4e^2$, exhibiting a series of quantized Hall resistance plateaus where the corresponding longitudinal resistance R_{zz}^x is strongly suppressed or vanishes. This behavior resembles the quantum Hall effect (Supplementary Note I), and thus features the emergence of high-quantized topological states originating from the spatial confinement^{48,49}.

Remarkably, the reversal of the Hall resistance in 3D QAHE represents a binary states of 0's and 1's, enabling a novel logic architecture as a unit cell in computational technology. Moreover, since the Hall resistance is intimately bound to the Fermi energy, which can be finely adjusted through a top gate without incorporation of external magnetic field or disturbing the system, this 3D QAHE thus provides a promising platform for the in-memory computing where the data storage and computation can be operated in parallel within the same physical location^{50,51}. As illustrated in Fig. 4b, in a 3D QAHE system with a top gate (magenta blocks) as well as four metallic leads (green blocks) attached one-by-one to each lateral surfaces, an applying current I_0 along z direction can trigger a Hall voltage V_h that depends on the Fermi energy E_f , forming a unit cell for realizing the in-memory computing. In this unit cell, the data retrieval (read) and processing (write) can be achieved in parallel through the top gate (write) and the Hall voltage V_h (read). Connecting this unit cell in series as schematically shown in Fig. 4c enables a multiple computational technology, in which each unit cell can be operated independently. Our calculations (Supplementary Note 6) verify that The Hall resistances in this multiple computational technology verily obey the straightforward relation $R_h^{\alpha=1,2}(= I_0/V_h^\alpha) = \text{sign}(E_f^\alpha)h/e^2$ when E_f^1 and E_f^2 both lie within the inverted band gap, demonstrating the reliability of this strategy. Most importantly, owing to the absence of backscattering, the current required to drive this multiple computational process is the same as that in one unit cell. Thus, this in-memory computational scheme is favorably low energy consuming, which is extremely feasible for next-generation computing requiring intensive data processing such as artificial intelligence.

Discussion

The realization of this 3D QAHE relies heavily on the incorporation of Rashba spin-orbit coupling into the WSM harboring two pairs of shifted Weyl nodes. Given that many WSMs have been proposed and also confirmed in experiment extensively^{7,11,12}, our theory could possibly be tested in magnetically doped type-I WSMs, such as Fe, Cr, V doped Cd₃As₂⁵² or Na₃Bi⁵³, which possess two pair of Weyl nodes if the time reversal symmetry is breaking. Sizable spin-orbit coupling and energy split can be achieved through the coupling between the itinerant electrons within these WSMs and 3d electrons in doped magnetic atoms. On the other hand, there is also a chance that our theory could be realized in other WSMs with multi-pairs of Weyl nodes when including energy split λ and the Rashba spin-orbit coupling, which may hosts high Chern number 3D QAHE because of the multiple surface bands.

In conclusion, we have proposed a 3D QAHE existing on the surface of a cubic WSM when incorporating a conventional Rashba spin-orbit coupling. This 3D QAHE hosts two chiral surface states along x direction, a pair of Fermi energy dependent chiral hinge states along y direction, and also a pair of Fermi energy dependent chiral surface states along z direction. Those peculiar boundary states inherent to the 3D QAHE in turn results in a highly anisotropic transport behavior, where the Hall resistance can be zero, h/e^2 , or $\pm h/e^2$ at different Fermi energies. The novel transport properties make this 3D QAHE an ideal platform for in-memory computing. Our work extends the scope of the QAHE, paving the way for the application of topological materials.

Methods

Analytical expression for the 3D Hamiltonian in momentum space. Under open boundary conditions along all three spatial directions, the analytical expression for the Hamiltonian described by Eq. (1) in the momentum space can be obtained by using the Fourier transformation, which takes the form

$$H = -\lambda\Gamma^1 - 2t_s \sin k_x \Gamma^5 + 2it_s \sin k_y \Gamma^1 \Gamma^5 - 2iA \sin k_z \Gamma^2 \Gamma^5 - 2iA \sin k_y \Gamma^3 \Gamma^5 + i(4m - 2m_x \cos k_x - 2m \cos k_y - 2m \cos k_z) \Gamma^4 \Gamma^5, \quad (3)$$

where the Dirac Γ matrices are $\Gamma^{1,2,3,4,5} = (\sigma_z \otimes I_2, i\sigma_y \otimes \tau_x, i\sigma_y \otimes \tau_y, i\sigma_y \otimes \tau_z, \sigma_x \otimes I_2)$. Note that these Dirac Γ matrices satisfy the Clifford algebra and the anticommutation relations $\{\Gamma^\alpha, \Gamma^\beta\} = 2\eta^{\alpha\beta} I_4$ with $\eta_{\alpha\beta} = \text{diag}(1, -1, -1, -1)$, where $\Gamma^{1,5}$ are Hermitian while $\Gamma^{2,3,4}$ are anti-Hermitian. The eigenenergy of the Hamiltonian in Eq. (3) is $E(\mathbf{k}) = \pm \sqrt{(a \pm d)^2 + b^2 + c^2}$ where $a = \sqrt{4A^2(\sin^2 k_y + \sin^2 k_z) + [4m - 2m_x \cos k_x - 2m(\cos k_y - \cos k_z)]^2}$, $b = -2t_s \sin k_x$, $c = -2t_s \sin k_y$, and $d = -\lambda$.

Calculation of band Chern number on a slab. The Hamiltonian in Eq. (1) can be rewritten as

$$H = c_n^\dagger t_0 c_n + (c_n^\dagger t_x c_{n+\delta_x} + c_n^\dagger t_y c_{n+\delta_y} + c_n^\dagger t_z c_{n+\delta_z} + \text{h.c.}), \quad (4)$$

where the hopping matrices $t_0 = -4m\tau_z \otimes \sigma_z - \lambda\sigma_z$, $t_x = m_x\tau_z \otimes \sigma_z + it_s\sigma_x$, $t_y = m\tau_z \otimes \sigma_z - iA\tau_y \otimes \sigma_z + it_s\sigma_y$, $t_z = m\tau_z \otimes \sigma_z - iA\tau_x \otimes \sigma_z$. On a slab, we can perform a Fourier transformation with respect to the lateral directions, for example α and β directions, which recasts the Hamiltonian as

$$H(k_\alpha, k_\beta) = c_n^\dagger [t_0 + (t_\alpha e^{ik_\alpha} + t_\beta e^{ik_\beta} + \text{h.c.})] c_n + (c_n^\dagger t_\gamma c_{n+\delta_\gamma} + \text{h.c.}), \quad (5)$$

where γ is another direction perpendicular to both α and β . The Chern number on this slab can then be calculated by using the TKNN formula¹⁹

$$\mathcal{C}_{\alpha\beta} = \frac{1}{\pi} \sum_{E_m < E_f < E_n} \int dk_\alpha dk_\beta \text{Im} \frac{\langle \psi_m | \partial_{k_\alpha} H(k_\alpha, k_\beta) | \psi_n \rangle \langle \psi_n | \partial_{k_\beta} H(k_\alpha, k_\beta) | \psi_m \rangle}{(E_m - E_n)^2}, \quad (6)$$

where $E_{m(n)}$ is the eigenenergy of $H(k_\alpha, k_\beta)$ in Eq. (5) with $|\psi_{m(n)}\rangle$ corresponding eigenfunction.

Data availability

The data that support the plots within this paper and other findings of this study are available from the corresponding author upon reasonable request. Source data are provided with this paper.

Code availability

The code that is deemed central to the conclusions is available at ...

References

1. Hasan, M. Z. & Kane, C. L. Colloquium: Topological insulators. *Rev. Mod. Phys.* **82**, 3045–3067 (2010).
2. Qi, X. L. & Zhang, S. C. Topological insulators and superconductors. *Rev. Mod. Phys.* **83**, 1057–1110 (2011).
3. Shen, S.-Q. *Topological Insulators: Dirac Equation in Condensed Matters*, vol. 174 of *Springer Series in Solid-State Sciences* (Springer Berlin, Heidelberg, 2012).
4. Chang, C.-Z., Liu, C.-X. & MacDonald, A. H. Colloquium: Quantum anomalous Hall effect. *Rev. Mod. Phys.* **95**, 011002 (2023).
5. Chiu, C.-K., Teo, J. C. Y., Schnyder, A. P. & Ryu, S. Classification of topological quantum matter with symmetries. *Rev. Mod. Phys.* **88**, 035005 (2016).
6. Moore, J. E. The birth of topological insulators. *Nature* **464**, 194–198 (2010).
7. Yan, B. & Felser, C. Topological Materials: Weyl Semimetals. *Annu. Rev. Condens. Matter Phys.* **8**, 337–354 (2017).
8. Senthil, T. Symmetry-Protected Topological Phases of Quantum Matter. *Annu. Rev. Condens. Matter Phys.* **6**, 299–324 (2015).
9. Hasan, M. Z. & Moore, J. E. Three-Dimensional Topological Insulators. *Annu. Rev. Condens. Matter Phys.* **2**, 55–78 (2011).
10. Tokura, Y., Yasuda, K. & Tsukazaki, A. Magnetic topological insulators. *Nat. Rev. Phys.* **1**, 126–143 (2019).

11. Armitage, N. P., Mele, E. J. & Vishwanath, A. Weyl and Dirac semimetals in three-dimensional solids. *Rev. Mod. Phys.* **90**, 015001 (2018).
12. Lv, B. Q., Qian, T. & Ding, H. Experimental perspective on three-dimensional topological semimetals. *Rev. Mod. Phys.* **93**, 025002 (2021).
13. Hasan, M. Z., Xu, S.-Y., Belopolski, I. & Huang, S.-M. Discovery of Weyl Fermion Semimetals and Topological Fermi Arc States. *Annu. Rev. Condens. Matter Phys.* **8**, 289–309 (2017).
14. von Klitzing, K. *et al.* 40 years of the quantum Hall effect. *Nat. Rev. Phys.* **2**, 397–401 (2020).
15. Yoshioka, D. *The Quantum Hall Effect*, vol. 133 of *Springer Series in Solid-State Sciences* (Springer Berlin, Heidelberg, 2002).
16. Burkov, A. A. Topological semimetals. *Nat. Mater.* **15**, 1145–1148 (2016).
17. Haldane, F. D. M. Model for a Quantum Hall Effect without Landau Levels: Condensed-Matter Realization of the "Parity Anomaly". *Phys. Rev. Lett.* **61**, 2015–2018 (1988).
18. Chang, C.-Z. *et al.* Experimental Observation of the Quantum Anomalous Hall Effect in a Magnetic Topological Insulator. *Science* **340**, 167–170 (2013).
19. Thouless, D. J., Kohmoto, M., Nightingale, M. P. & den Nijs, M. Quantized Hall Conductance in a Two-Dimensional Periodic Potential. *Phys. Rev. Lett.* **49**, 405–408 (1982).
20. Checkelsky, J. G. *et al.* Trajectory of the anomalous Hall effect towards the quantized state in a ferromagnetic topological insulator. *Nat. Phys.* **10**, 731–736 (2014).
21. Hatsugai, Y. Chern number and edge states in the integer quantum Hall effect. *Phys. Rev. Lett.* **71**, 3697–3700 (1993).
22. Prodan, E. & Schulz-Baldes, H. *Bulk and Boundary Invariants for Complex Topological Insulators*. No. 1 b/w illustrations in *Mathematical Physics Studies* (Springer Cham, 2016), 1 edn. Published: 16 February 2016, Softcover Published: 30 March 2018, eBook Published: 05 February 2016.
23. Zhao, Y.-F. *et al.* 3D Quantum Anomalous Hall Effect in Magnetic Topological Insulator Trilayers of Hundred-Nanometer Thickness. *Adv. Mater.* **36**, 2310249 (2024).
24. Jin, Y. J., Wang, R., Xia, B. W., Zheng, B. B. & Xu, H. Three-dimensional quantum anomalous Hall effect in ferromagnetic insulators. *Phys. Rev. B* **98**, 081101 (2018).
25. Wang, C. M., Sun, H.-P., Lu, H.-Z. & Xie, X. C. 3D Quantum Hall Effect of Fermi Arcs in Topological Semimetals. *Phys. Rev. Lett.* **119**, 136806 (2017).
26. Li, H., Liu, H., Jiang, H. & Xie, X. C. 3D Quantum Hall Effect and a Global Picture of Edge States in Weyl Semimetals. *Phys. Rev. Lett.* **125**, 036602 (2020).
27. Chang, M., Geng, H., Sheng, L. & Xing, D. Y. Three-dimensional quantum Hall effect in Weyl semimetals. *Phys. Rev. B* **103**, 245434 (2021).

28. Ma, R., Sheng, D. N. & Sheng, L. Three-dimensional quantum Hall effect and magnetothermoelectric properties in Weyl semimetals. *Phys. Rev. B* **104**, 075425 (2021).
29. Tang, F. *et al.* Three-dimensional quantum Hall effect and metal–insulator transition in ZrTe_5 . *Nature* **569**, 537–541 (2019).
30. Zhang, C. *et al.* Quantum Hall effect based on Weyl orbits in Cd_3As_2 . *Nature* **565**, 331–336 (2019).
31. Zhang, C. *et al.* Evolution of Weyl orbit and quantum Hall effect in Dirac semimetal Cd_3As_2 . *Nat. Commun.* **8**, 1272 (2017).
32. Uchida, M. *et al.* Quantum Hall states observed in thin films of Dirac semimetal Cd_3As_2 . *Nat. Commun.* **8**, 2274 (2017).
33. Schumann, T. *et al.* Observation of the Quantum Hall Effect in Confined Films of the Three-Dimensional Dirac Semimetal Cd_3As_2 . *Phys. Rev. Lett.* **120**, 016801 (2018).
34. Wan, X., Turner, A. M., Vishwanath, A. & Savrasov, S. Y. Topological semimetal and Fermi-arc surface states in the electronic structure of pyrochlore iridates. *Phys. Rev. B* **83**, 205101 (2011).
35. Liu, Z. K. *et al.* Discovery of a Three-Dimensional Topological Dirac Semimetal, Na_3Bi . *Science* **343**, 864–867 (2014).
36. Lv, B. Q. *et al.* Experimental discovery of Weyl semimetal TaAs. *Phys. Rev. X* **5**, 031013 (2015).
37. Xu, S.-Y. *et al.* Discovery of a Weyl fermion semimetal and topological Fermi arcs. *Science* **349**, 613–617 (2015).
38. Lu, H.-Z., Zhang, S.-B. & Shen, S.-Q. High-field magnetoconductivity of topological semimetals with short-range potential. *Phys. Rev. B* **92**, 045203 (2015).
39. Burkov, A. A. & Balents, L. Weyl Semimetal in a Topological Insulator Multilayer. *Phys. Rev. Lett.* **107**, 127205 (2011).
40. Okugawa, R. & Murakami, S. Dispersion of Fermi arcs in Weyl semimetals and their evolutions to Dirac cones. *Phys. Rev. B* **89**, 235315 (2014).
41. Benalcazar, W. A., Bernevig, B. A. & Hughes, T. L. Quantized electric multipole insulators. *Science* **357**, 61–66 (2017).
42. Benalcazar, W. A., Bernevig, B. A. & Hughes, T. L. Electric multipole moments, topological multipole moment pumping, and chiral hinge states in crystalline insulators. *Phys. Rev. B* **96**, 245115 (2017).
43. Ezawa, M. Higher-order topological insulators and semimetals on the breathing kagome and pyrochlore lattices. *Phys. Rev. Lett.* **120**, 026801 (2018).

44. Schindler, F. *et al.* Higher-order topology in bismuth. *Nature Physics* **14**, 918–924 (2018).
45. Li, S., Gong, M., Li, Y.-H., Jiang, H. & Xie, X. C. High spin axion insulator. *Nature Communications* **15**, 4250 (2024).
46. Datta, S. *Electronic Transport in Mesoscopic Systems* (Cambridge University Press, Cambridge, England, 1995).
47. Halperin, B. I. Quantized Hall conductance, current-carrying edge states, and the existence of extended states in a two-dimensional disordered potential. *Phys. Rev. B* **25**, 2185–2190 (1982).
48. Cao, T., Zhao, F. & Louie, S. G. Topological phases in graphene nanoribbons: Junction states, spin centers, and quantum spin chains. *Phys. Rev. Lett.* **119**, 076401 (2017).
49. Rizzo, D. J. *et al.* Topological band engineering of graphene nanoribbons. *Nature* **560**, 204–208 (2018).
50. Tan, K.-L. *et al.* In-memory databases: Challenges and opportunities from software and hardware perspectives. *SIGMOD Rec.* **44**, 35–40 (2015).
51. Ghose, S., Boroumand, A., Kim, J. S., Gómez-Luna, J. & Mutlu, O. Processing-in-memory: A workload-driven perspective. *IBM Journal of Research and Development* **63**, 3:1–3:19 (2019).
52. Wang, Z., Weng, H., Wu, Q., Dai, X. & Fang, Z. Three-dimensional Dirac semimetal and quantum transport in Cd_3As_2 . *Phys. Rev. B* **88**, 125427 (2013).
53. Wang, Z. *et al.* Dirac semimetal and topological phase transitions in $A_3\text{Bi}$ ($A = \text{Na}, \text{K}, \text{Rb}$). *Phys. Rev. B* **85**, 195320 (2012).

Acknowledgements

We are grateful for the fruitful discussions with Q. Wei, M. Gong, C. Z. Chen and H. W. Liu. This work is financially supported by the National Basic Research Program of China (Grants No. 2019YFA0308403 and No. 2022YFA1403700), National Natural Science Foundation of China (Grants Nos. 12204044, 12147126 and 12404056). Y.H.L also acknowledge financial support from the Fundamental Research Funds for the Central Universities, the State Key Laboratory of Surface Physics and the Department of Physics at Fudan University

Author contributions

H.J. and X.C.X conceived the initial idea of 3D QAHE. Z.-Q.Z and Y.-H.L performed calculations with assistance from M.L.. All authors discussed the results. Z.-Q.Z. and Y.-H.L. wrote the manuscript with contributions from all authors. H.J. and X.C.X. supervised the project.

Competing interests

The authors declare no competing interests.

Additional information

Supplementary information The online version contains supplementary material available at .

Correspondence and requests for materials should be addressed to Hua Jiang.

Reprints and permissions information is available at <http://www.nature.com/reprints>

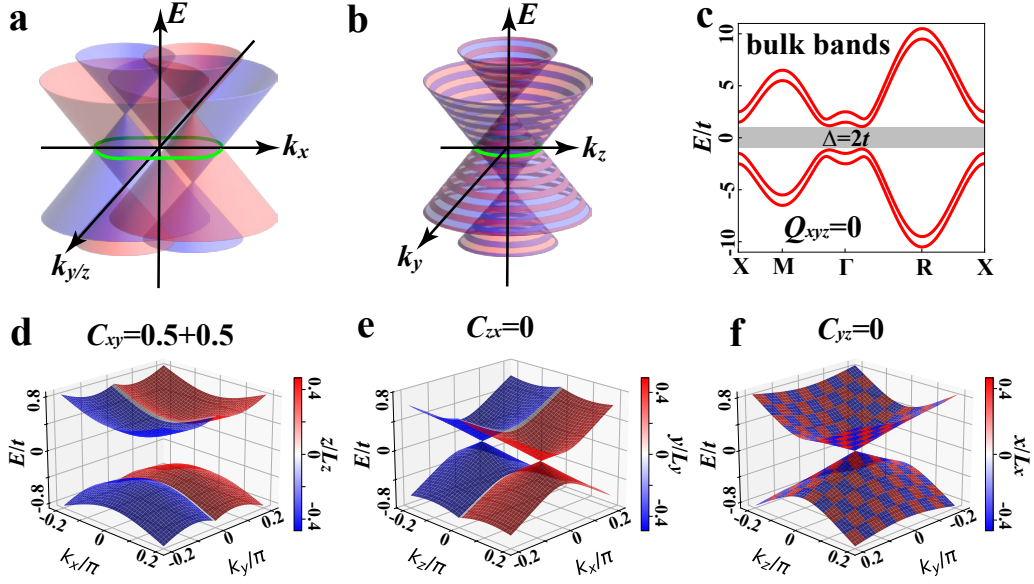


Figure 1: Proposal of the 3D QAHE. **a,b** Schematics for the band dispersions in the absence of spin-orbit coupling on $k_x - k_{y,z}$ plane **(a)** and $k_y - k_z$ plane **(b)**. The Weyl nodes at $\mathbf{k}_w = (\pm\pi, 0, 0)$ are shifted to $E_{\pm} = \pm\lambda$. The Green lines highlight the Fermi arc band at the charge neutral point ($E = 0$), which are doubly degenerated. **c** Bulk band structure of the system with Rashba spin-orbit coupling along $X \rightarrow M \rightarrow \Gamma \rightarrow R \rightarrow X$ trajectory in the first Brillouin zone. The gray shadow region denotes the bulk band gap of size $\Delta = 2t$. The octupole moment $Q_{xyz} = 0$ is labeled in the bottom. **d-f** Two-dimensional surface band spectra of a slab and corresponding wavefunction distributions on $k_x - k_y$ **(d)**, $k_z - k_x$ **(e)**, $k_y - k_z$ **(f)** planes, respectively. The band Chern numbers for each cases are labeled above. Here, the thickness of the slab is $L = 10$.

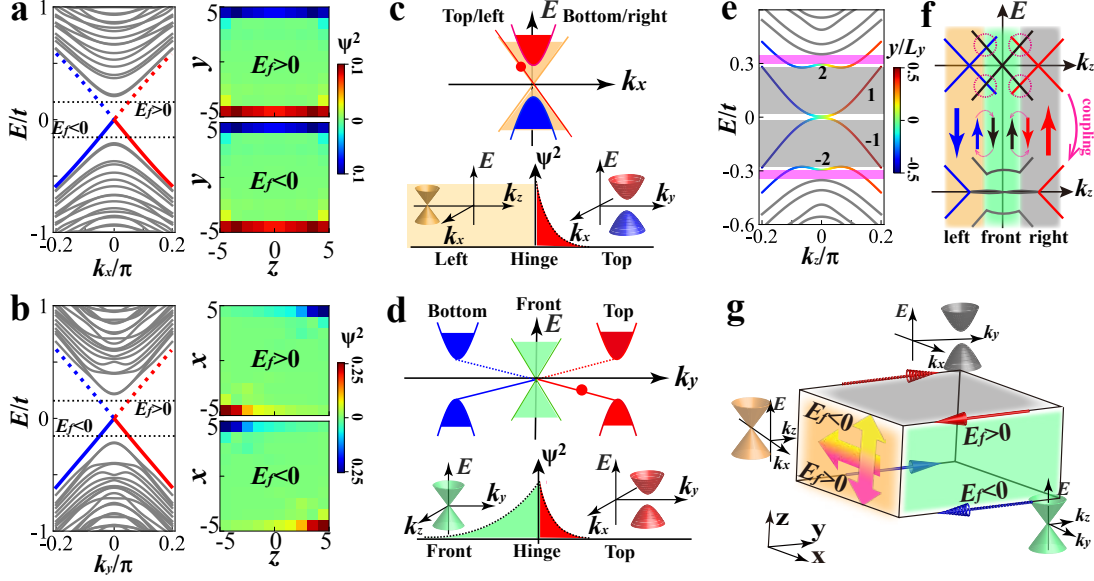


Figure 2: Bulk-boundary correspondence. **a,b** Band spectra on a one-dimensional nanowire (left panels). Gray (red and blue) lines represent the bulk (boundary) bands. Right panels display the wave function distributions on the cross-section of the nanowire for two representative Fermi energy indicated by the black dashed line in the left panels. The red and blue colors here represent the propagating direction identical to the group velocity. The system size is $L_{y/x} = L_z = 10$. **c,d** Schematic for the wavefunction distribution across the hinge into the neighboring surface along x (**c**) and y (**d**) directions. The gapless Dirac cone at center refers to the lateral surface band spectrum while the gaped Dirac cone represents the top (or bottom) surface band spectrum. **e** One-dimensional band structure on a nanowire extending infinitely along z direction and the average position $\langle y/L_y \rangle$. Separations between surface bands ± 1 (colorful lines) and ± 2 (colorful lines) or bulk band (gray lines) are highlighted in gray or magenta shadows. The system size is $L_x = L_y = 8$. **f** Schematic for the formation of chiral surface states along z direction. Top: schematic band spectrum without coupling among neighboring surfaces. The magenta circles highlight the band cross regions, where gap opening occurs when including the coupling among neighboring surface bands, resulting in a band structure displayed in the bottom. During this process, four chiral surface states (thin arrows) are eliminated while only two (thick arrows) survive. The background in different colors represents different surfaces. **g** Edge picture of the 3D QAHE. Here, extended thick arrows refer to extended surface states propagating along the arrow direction while line arrows represent the hinge states. The surface band dispersions are plotted on each surface.

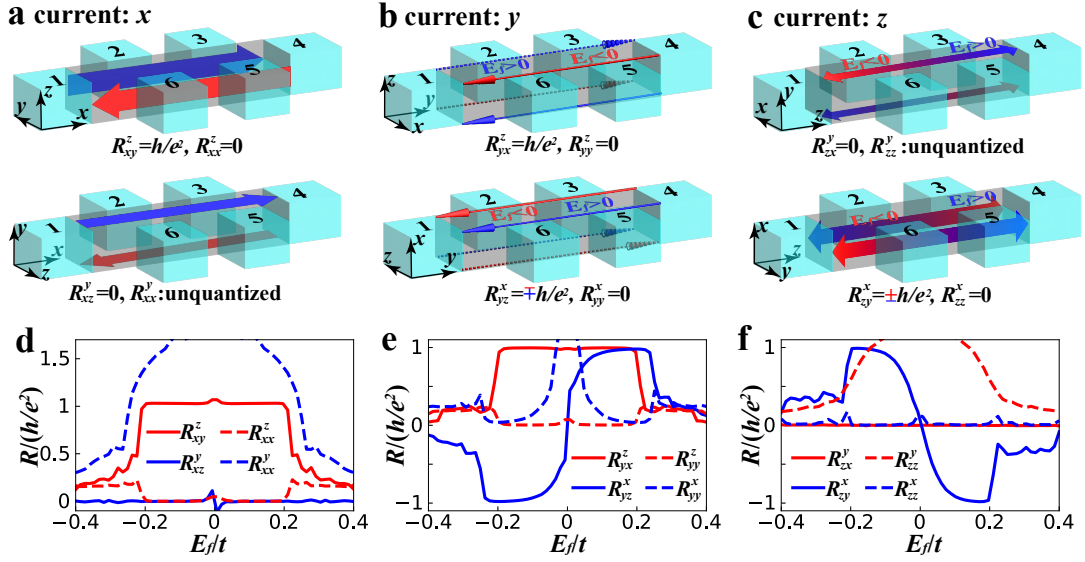


Figure 3: Transport properties of 3D QAHE. **a,b,c** Six different hallbar configurations in three dimensions and corresponding edge states (colorful arrows) at different Fermi energy E_f . Hall resistance and longitudinal resistance for each configuration obtained from the edge picture analysis are labeled below. **d,e,f** Hall resistances (solid lines) and longitudinal resistances (dashed lines) versus the Fermi energy E_f for different Hall bar configurations calculated by using Green's function method. Here, the size for all six metallic leads in each Hall bar is 10×10 , and the distance between neighboring leads is $L = 20$. All data are obtained in the presence of a random disorder with strength $W = 0.5t$ under 100 times ensemble average.

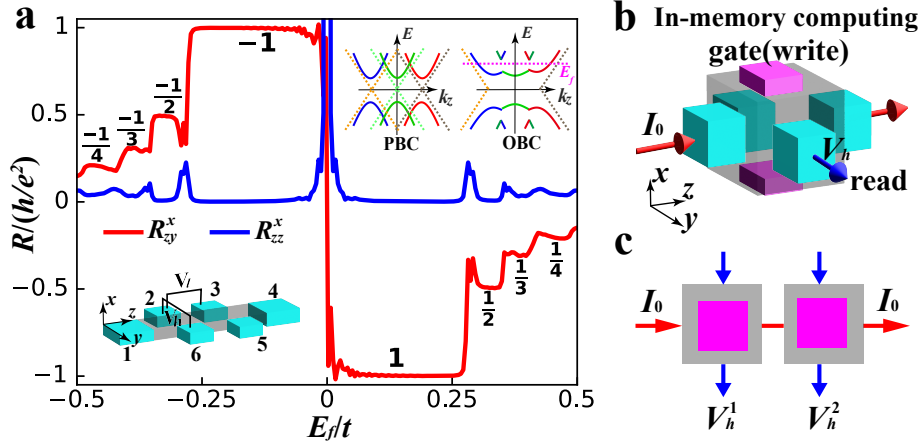


Figure 4: Fractional-quantized Hall resistance and strategy for in-memory computing. **a** R_{zy}^x and R_{zz}^x versus the Fermi energy E_f . Top right panel illustrates the gap opening due to the coupling between neighboring surface bands. Bottom left panel shows a Hall bar configuration with V_l (V_h) the longitudinal (Hall) voltage. **b** A unit cell for in-memory computing based on 3D QAHE. The green blocks refer to the metallic leads and the magenta blocks denote the top gate. I_0 is the applied current along z direction, V_h is the Hall voltage. **c** Two computational unit cells are connected in series. Each unit cell can be operated independently.

Supplementary Information for “Three-dimensional quantum anomalous Hall effect in Weyl semimetals”

Zhi-Qiang Zhang^{1,2,8}, Yu-Hang Li^{3,8}, Ming Lu⁴, Hongfang Liu², Hailong Li^{1,5}, Hua Jiang¹✉, and X. C. Xie^{1,5,6}

¹*Interdisciplinary Center for Theoretical Physics and Information Sciences (ICTPIS), Fudan University, Shanghai 200433, China*

²*School of Physical Science and Technology, Soochow University, Suzhou 215006, China*

³*School of Physics, Nankai University, Tianjin 300071, China*

⁴*State Key Laboratory of the Surface Physics and Department of Physics, Fudan University, 200433, Shanghai, China*

⁵*Beijing Academy of Quantum Information Sciences, Beijing 100193, China*

⁶*International Center for Quantum Materials, School of Physics, Peking University, Beijing 100871, China*

⁷*Hefei National Laboratory, Hefei 230088, China*

Contents

Introduction to the Supplementary Information	3
Note 1: Comparison between quantum Hall effect and emergent topology in 3D QAHE	3
Note 2: Band properties of the 3D QAHE	5
A. Construction of the 3D QAHE	5
B. Momentum-surface locking	6
C. Surface band structure	6
D. Layer-resolved Chern number	8
Note 3: Landauer-Büttiker theory for the transport in 3D QAHE	9
Note 4: Effective model for the surface states	10
Note 5: Chiral boundary states with quantized Chern number on x-y plane	13
A. Numerical results: wave function distributions	13
B. Half-integer-Chern-number-difference induced bound states	14
Note 6: Multiple unit-cell for in-memory computing	17

⁸These authors contributed equally to this work: Zhi-Qiang Zhang and Yu-Hang Li.
✉email:jianghuaphy@fudan.edu.cn.

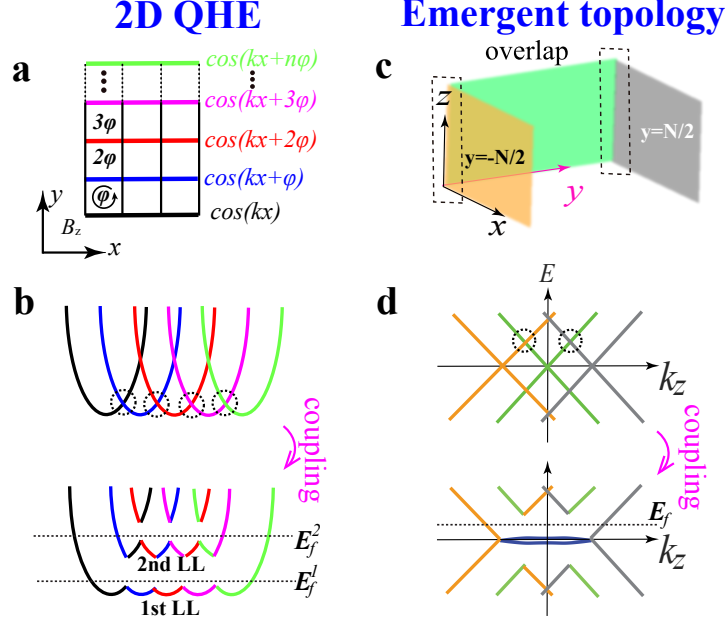
Introduction to the Supplementary Information

In this Supplementary Materials, we present more details about the 3D QAHE proposed in the main text. In Supplementary Note 1, we provide an intuitive picture for understanding the emergent topology our in the 3D QAHE by comparing it with the renowned quantum Hall effect on a two-dimensional square lattice. In Supplementary Note 2, we provide more details about the band properties of the 3D QAHE, including the motivation to construct this 3D QAHE from three-dimensional WSM (Supplementary Note 2A), the inherent momentum-surface locking (Supplementary Note 2B), the surface band structure (Supplementary Note 2C) and the layer-resolved Chern number (Supplementary Note 2D). In Supplementary Note 3, we present the numerical detail on the Landauer-Büttiker theory for calculating the transport behavior of the 3D QAHE. Supplementary Note 4 gives the effective surface Hamiltonian for the 3D QAHE along different directions. In Supplementary Note 5, we further elucidates the existence of boundary states triggered by the Chern number difference among neighboring surfaces. Finally in Supplementary Note 6, we present the numerically simulation of the Hall voltages when manipulating the top gates that can be used in in-memory computing.

Note 1: Comparison between quantum Hall effect and the emergent topology in 3D QAHE

In this section, we provide an intuitive picture to understand the emergent boundary states along z direction in the 3D QAHE by comparing it with the renowned two-dimensional quantum Hall effect. As depicted in Supplementary Fig. 1a, a two-dimensional square lattice with open boundary condition along y direction can be effectively viewed as a series of coupled one-dimensional electron chains. Each chain along x direction has a band dispersion $E(k) \sim \cos(kx)$ in the absence of both magnetic field as well as the coupling among them through the bond along y direction. In the presence of a strong perpendicular magnetic field, each unit cell acquires a magnetic flux ψ . Therefore, the band of one-dimensional chain at finite y is shifted consecutively as shown in Fig. 1a, leading to an overall shifted band structure intersecting with each other as schematically displayed in the top panel in Supplementary Fig. 1b. Furthermore, turning on the coupling among these chains through the y bond opens gaps near the band cross regimes and thus gives rise to the profound Landau levels shown in the bottom panel. When the Fermi level lies in between two Landau levels, for example between the first and second Landau levels, the Hall conductance is identical to the number of the edge states determined through the intersection between Landau levels and the Fermi energy.

The emergent topology along z direction in our proposal of the 3D QAHE can be understood in the same token. Under periodic boundary condition along the lateral directions, the surface states on left and right surfaces are shifted oppositely along k_z direction by the momentum-surface locking, while the front and back surface states persists, which results in a resembling shifted band structure intersecting with each other as illustrated in Fig. 1c. Under open boundary condition, the neighboring surface states can couple with each other through

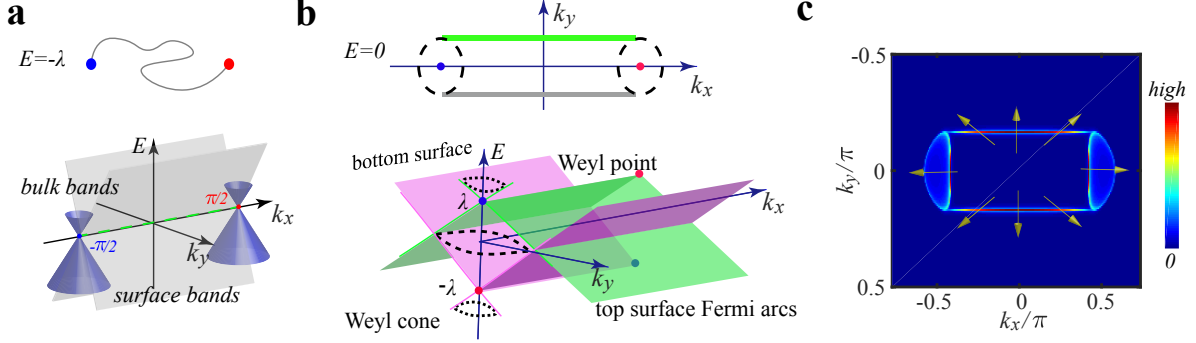


Supplementary Fig. 1: Comparison between 2D QAHE and emergent topology in 3D QAHE. **a, b,** An intuitive picture for the renowned quantum Hall effect on a two-dimensional square lattice. Each horizontal line along x direction in **a** represents a one-dimensional chain with a band dispersion $E(k) \sim \cos(kx)$. Imposing a magnetic field introduces a magnetic flux ϕ enclosed by each square lattice, which shifts the one-dimensional chain along y direction consecutively and thus leads to a band structure illustrated in the top panel in **b**. Further including the coupling among those one-dimensional chains through the bond along y direction opens gaps near the band cross regimes highlighted by the black dashed circles, resulting in a band structure with the emergence of Landau levels as shown in the bottom panel. Here, LL is the shorthand for Landau level. **c** and **d** show the picture of the emergent topology along z direction in the 3D QAHE. In the periodic boundary condition along x and/or y directions, the band structure along k_z consists of three Dirac cones near the charge neutral point as indicated by the solid lines in **c**, where the central line bands refer to the coincident front and back surfaces that are doubly degenerated while the cadmium orange lines and the brown lines refer to the oppositely shifted left and right surfaces. The dashed lines represents the high energy parabolic bands on different surfaces. In the open boundary conditions along both x and y directions, the coupling between neighbor surfaces through the common hinge opens gaps near the band cross regimes, resembling the two-dimensional quantum Hall effect shown in **a** and **b**. This gives rise to a band structure illustrated in **d** even though the side surface Chern numbers are all zero.

the common hinges, which thus opens band gaps near the cross regimes, and simultaneously, gives rise to a band structure in analogy to the Landau levels as shown in Fig. 1d. Since the survived chiral states indicated by brown and yellow lines are fully confined to the boundary of the system, the Hall conductance in this case also equals to the number of these boundary states that intersect with the Fermi energy E_f .

Note 2: Band properties of the 3D QAHE

A. Construction of the 3D QAHE



Supplementary Fig. 2: Construction of 3D QAHE. **a** Schematic band structure for a Weyl semimetal with two Weyl nodes. The top panel displays a cartoon of the degenerated Fermi arc connecting these two Weyl nodes. **b** Schematic band structure on k_x - k_y plane for a Weyl semimetal with two pairs of Weyl nodes. Non-degenerated Fermi arcs are illustrated in the top panel, which forms a close manifold at the charge neutral point with $E = 0$. **c** The spectrum function $A(k_x, k_y) = -\text{Im}[E + i0^+ - \mathcal{H}]^{-1}/\pi$ for our model Hamiltonian with $E = t_s = 0$, $\lambda = 0.5t$. The yellow arrows represent the spin directions ($\langle \sigma \rangle$) at different momenta with $t_s \neq 0$.

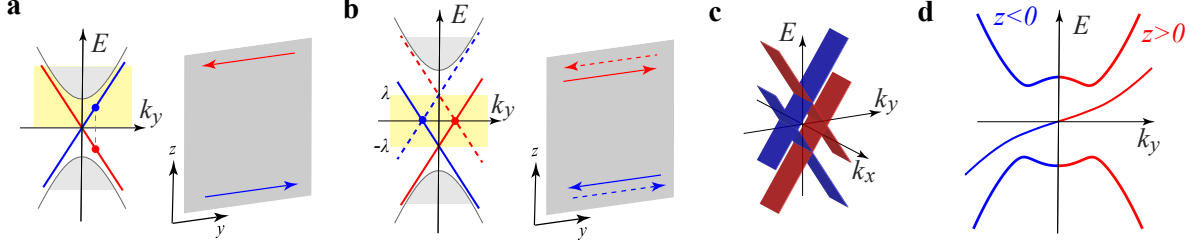
The key ingredient for realizing the 3D QAHE relies on the construction of two-dimensional inverted band structure in the first Brillouin zone. The surface band of a Weyl semimetal provides a natural platform as those surface bands are extended on two-dimensional surfaces of a three-dimensional system. However, since a Weyl semimetal with only two Weyl nodes described by \mathcal{H}_w possesses only one open Fermi arc as displayed in Supplementary Fig. 2a, which is inadequate to define a quantized Chern number, the minimum Hamiltonian to construct a 3D QAHE in Weyl semimetals must possess two pairs of non-degenerated Weyl nodes. In this case, the non-degenerated Fermi arcs can form a closed manifold that are doubly degenerated as shown in Supplementary Fig. 2b, which enables us to define a quantized Chern number. Consequently, the minimum Hamiltonian for this system takes the form

$$\mathcal{H} = \begin{pmatrix} \mathcal{H}_w - \lambda & f(t_s) \\ f^\dagger(t_s) & -\mathcal{H}_w + \lambda \end{pmatrix} = (\mathcal{H}_w - \lambda)\sigma_z + [it_s(\sigma_x c_n^\dagger c_{n+\delta_x} + \sigma_y c_n^\dagger c_{n+\delta_y}) + h.c.], \quad (1)$$

where λ refers to a Zeeman term used to break the degeneracy of the Fermi arcs, $f(t_s)$ and $f^\dagger(t_s)$ are Rashba spin-orbit coupling (SOC) that couple \mathcal{H}_w with $-\mathcal{H}_w$. In the absence of the Zeeman term and the SOC ($\lambda = t_s = 0$), the model Hamiltonian in Supplementary Eq. (1) describes a Weyl semimetal with four degenerated Weyl nodes. Including the Zeeman term splits these four Weyl nodes and thus breaks the degeneracy, resulting in a band structure shown in the bottom panel in Supplementary Fig. 2b. In this case, the Weyl nodes intersect at finite momentum, which thus forms a closed manifold on k_x - k_y plane as shown in the top

panel in Supplementary Figs. 2b and c. Further including the SOC opens a band gap near the charge neutral point around $E \sim 0$, which thus gives rise to the 3D QAHE characterized by the quantized Chern number $\mathcal{C} = 1$.

B. Momentum-surface locking

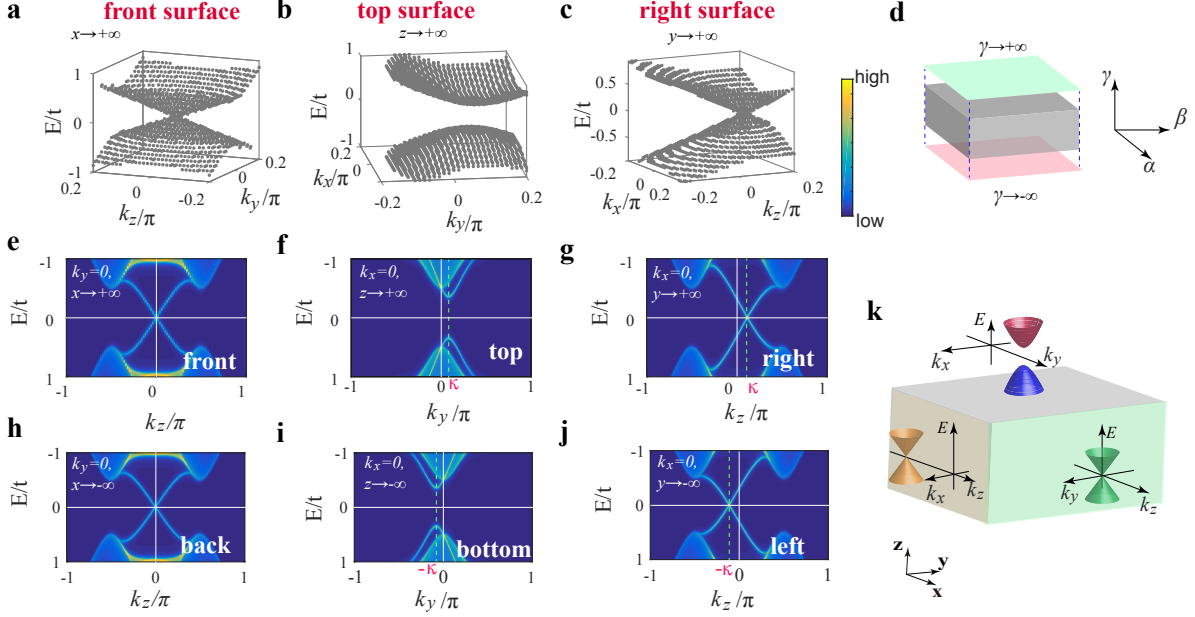


Supplementary Fig. 3: Momentum-surface locking. Schematic one-dimensional band dispersion along k_y direction (left panels) and boundary states (right panels) for a Weyl semimetal with one pair of Weyl nodes (**a**, Hamiltonian \mathcal{H}_{WSM}) and two pairs of Weyl nodes with an energy split [**b**, Hamiltonian $(\mathcal{H}_{WSM} - \lambda)\sigma_z$]. The gray regimes represent the bulk bands while the colorful lines refer to the surface states. The term $\lambda\sigma_z$ shifts one Weyl node upwards while the other one downwards as depicted in **b**. This two shifted Weyl nodes intersect at the charge neutral point at finite k_y , resulting in two new Dirac cones at $E = 0$ that are bound to the real space locations. The red Dirac cone locates at the top boundary whereas the blue Dirac cone locates oppositely at the the bottom boundary. **c** Two-dimensional band dispersion on k_x - k_y plane with momentum-surface locking, where the red states are confined to one surface while the blue bands are confined to the opposite surface. **d** One-dimensional band dispersion for the 3D QAHE. The red (blue) states locate at the surface with positive (negative) z .

To clarify the momentum-surface locking, we project the band structure to k_y direction. As illustrated in Supplementary Fig. 3a, each Weyl node has two boundary states with opposite chirality near the two termination along z direction. Due to the $\lambda\sigma_z$ term, the degenerated Weyl nodes are split as shown in Supplementary Fig. 3b, and these shifted Weyl nodes intersect again at $E = 0$ but with finite momenta, leading to two new Dirac cones at positive and negative momenta, respectively. In this circumstance, the boundary states corresponding to the red band in the left panel in Supplementary Fig. 3b are fully confined to the top surface at $z > 0$ (right panel in Supplementary Fig. 3b) and vice versa. Consequently, the location of these boundary states are bound to the momentum k_y as well as the Fermi energy E_f , exhibiting a momentum-surface locking that is crucial for the realization of 3D QAHE and is also instructive for understanding the unique bulk-boundary correspondence therein.

C. Surface band structure

To clarify the surface bands, we consider a semi-infinite slab extended semi-infinitely along one of the two perpendicular directions while still adopt periodic boundary conditions along



Supplementary Fig. 4: Surface band spectra. Surface band spectra for the front surface on k_y - k_z plane (a), the top surface on k_x - k_y plane (b), the right surface on k_z - k_x plane (c). d Schematic for a slab and the surface states. e-j One-dimensional surface state for different surfaces. The surface states on top, bottom, left and right surfaces are shifted due to the momentum surface locking while those on the front and back surfaces remain centered at the Γ point ($k_z = 0$). k Cartoon for the overall surface states of the system in the absence of coupling among them.

two lateral directions. This geometry preserves the translation symmetry along the lateral directions and most importantly, hosts only one surface state that can be revealed by the spectrum function defined as [1]

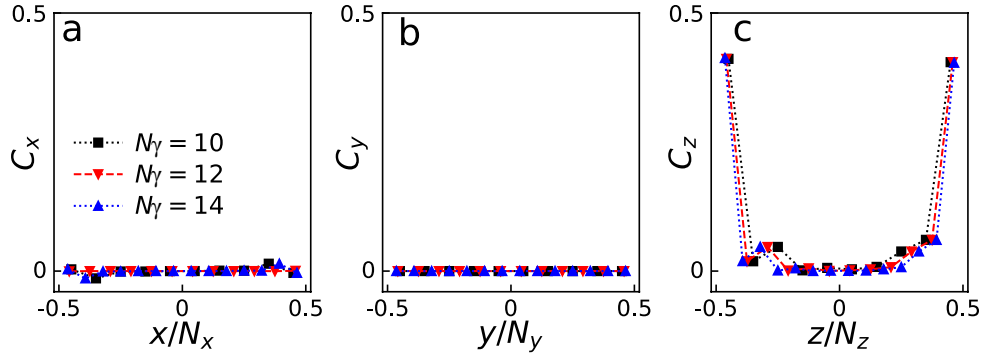
$$A(E, k_\alpha, k_\beta) = -\frac{1}{\pi} \text{Im}[E + i\eta - \mathcal{H}(k_\alpha, k_\beta)]^{-1}, \quad (2)$$

where $\mathcal{H}(k_\alpha, k_\beta)$ is the Hamiltonian of the system with k_α and k_β being the momenta on the lateral directions, and $\eta \rightarrow 0^+$ is the linewidth function. This equation can be solved iteratively since the system extends semi-infinitely along the perpendicular direction γ . The surface band spectra for the front, top, and right surfaces are shown in Figs. 4a-c, respectively. We see that the top surface band in Fig. 4b is clearly gaped while the front and right surface bands in Figs. 4a and c are gapless. Besides, the Dirac points of the top and right surface bands in Figs. 4b and c are shifted.

To further visualize the location of these surface states, we next explore the band spectra along one particular momentum by projecting the spectrum function along this momentum direction. Supplementary Figs. 4e and h show that the Dirac points of the front and back surface bands locate exactly at $k_z = 0$. Nevertheless, Supplementary Figs. 4f and i show that the gaped Dirac band on the top surface moves to the positive k_y direction while that on the bottom surface moves to the opposite negative k_y direction. Similarly, we find that the gapless Dirac bands on the left and right surface moves oppositely along k_z direction.

This affirms the momentum surface locking. We also ascertain that these Dirac bands locate exactly at the Γ point along the other momentum direction. Finally, the surface states are schematically summarized in Supplementary Fig. 4k, where the top and bottom surface states are gaped with momentum-surface locking, the left and right surface states are gapless with momentum-surface locking, while the front and back surfaces are gapless without momentum-surface locking.

D. Layer-resolved Chern number



Supplementary Fig. 5: Layer-resolved Chern numbers. Layer-resolved Chern numbers C_x [a], C_y [b], C_z [c] along different directions with different thickness $L_\gamma = 10$ (black square), 12 (red inverted triangle), 14 (blue triangle), respectively.

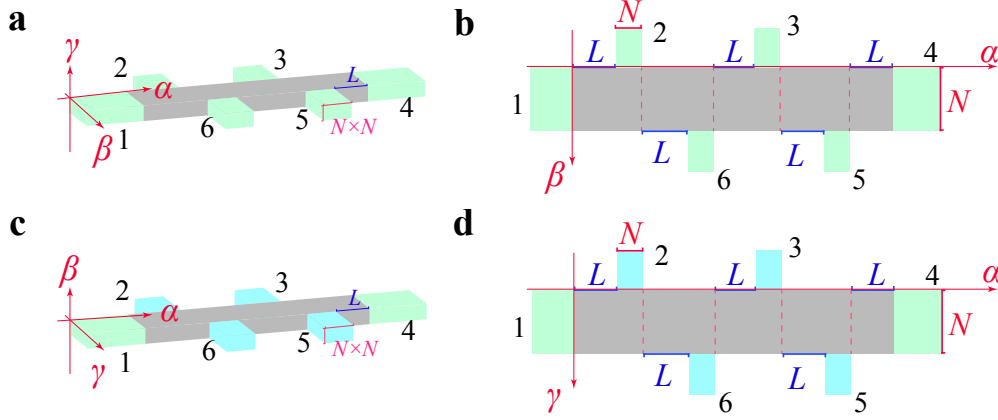
To elucidate the band topology, we resort to the TKNN formula to calculate the Chern numbers. In particular, we calculate the layer-resolved Chern number along different direction to gain more insight into the system, which can be obtained by projecting the band Chern number on a slab into each layer giving by the equation [2]

$$\mathcal{C}_{\alpha,\beta}(\gamma) = \frac{1}{\pi} \sum_{E_m < E_f < E_n} \int dk_\alpha dk_\beta \text{Im} \frac{\langle m | \hat{P}_\gamma \partial_{k_\alpha} \hat{H}(k_\alpha, k_\beta) | n \rangle \langle n | \partial_{k_\beta} \hat{H}(k_\alpha, k_\beta) | m \rangle}{(E_m - E_n)^2}, \quad (3)$$

where α, β represent the lateral directions, γ is the layer index, $\hat{P}_\gamma = |\gamma\rangle\langle\gamma|$ is the projecting operator, E_m (E_n) is the eigenenergy below (above) the Fermi energy E_f with $|m\rangle$ ($|n\rangle$) corresponding eigenstate, and Im refers to the imaginary part.

The results displayed in Supplementary Fig. 5 show that the Chern numbers on the side surfaces [\mathcal{C}_x in (a) and \mathcal{C}_y in (b)] are all zero. However, the Chern numbers on the top and bottom surfaces indicated by \mathcal{C}_z in Supplementary Fig. 5c are non-vanishing despite that these Chern numbers in the bulk are still zero. Our calculation show that both the top and bottom surface Chern numbers are $\mathcal{C}_{surf} = 0.5$, which gives rise to a combined Chern number $\mathcal{C} = 1$. Moreover, the Chern numbers on the side surfaces are all zero. This quantized Chern number unambiguously demonstrates a QAHE confined on the vertical surface of the 3D Weyl semimetal.

Note 3: Landauer-Büttiker theory for the transport in 3D QAHE



Supplementary Fig. 6: Hallbar setup and system size. Two hallbar configurations for calculating the Hall and longitudinal resistances. The size of all metallic leads is $L_\alpha \times L_\beta = N \times N$,

In this section, we provide the details for calculating the transport properties of the 3D QAHE on the six terminal Hallbar configuration. Supplementary Figs. 6 a and c show two different Hallbar configurations adopted in the main text. The two configurations are the same except that the transverse leads are attached on different surface. In both cases, a fixed current I_α is applied along α direction. Since the current in this system obeys the Kirchhoff's Law, the voltage drops on different leads can be obtained by using the Landauer-Büttiker formula [1, 4]:

$$\begin{pmatrix} T_1 & -T_{12} & -T_{13} & -T_{14} & -T_{15} & -T_{16} \\ -T_{21} & T_2 & -T_{23} & -T_{24} & -T_{25} & -T_{26} \\ -T_{31} & -T_{32} & T_3 & -T_{34} & -T_{35} & -T_{36} \\ -T_{41} & -T_{42} & -T_{43} & T_4 & -T_{45} & -T_{46} \\ -T_{51} & -T_{52} & -T_{53} & -T_{54} & T_5 & -T_{56} \\ -T_{61} & -T_{62} & -T_{63} & -T_{64} & -T_{65} & T_6 \end{pmatrix} \begin{pmatrix} V \\ V_2 \\ V_3 \\ -V \\ V_5 \\ V_6 \end{pmatrix} = \begin{pmatrix} I_\alpha \\ 0 \\ 0 \\ -I_\alpha \\ 0 \\ 0 \end{pmatrix}, \quad (4)$$

where V ($-V$) is the voltage potential on lead-1 (lead-4), V_n are the voltages on the transverse lead- n with $n \in [2, 3, 5, 6]$, and T_{mn} is the transmission coefficient from lead- n to lead- m . This transmission coefficient obeys the relation $T_{nn} = \sum_{m \neq n} T_{n,m}$ due to the current conservation where $T_{n,m}$ can be calculated by using the Green's function method [1]:

$$T_{nm} = \text{Tr}[\Gamma_n G^r(E_f) \Gamma_m G^a(E_f)]. \quad (5)$$

Here, $\Gamma_n = -i[\Sigma_n^r - \Sigma_n^a]$ is the line width function with Σ_n^r the self energy, $G^r(E_f) = [G^a(E_f)]^\dagger = (E_f + i\eta - \mathcal{H} - \sum_n \Sigma_n)$ is the retarded Green's function with \mathcal{H} the model Hamiltonian shown in Eq.(4) in the main text. Furthermore, the local current density from site i to site j is defined as [2]:

$$\mathbf{J}_{i \rightarrow j} = \frac{2e^2 V}{h} \text{Im}[H_{i,j} (G^r \Gamma_1 G^a)_{j,i}], \quad (6)$$

where V is the applied voltage and $H_{i,j}$ is the coupling Hamiltonian between site \mathbf{i} and site \mathbf{j} . In our calculations, we set $\Sigma_{n/m} = -i\mathcal{I}_{N^2 \times N^2}$, representing the metallic lead. Here $\mathcal{I}_{N^2 \times N^2}$ is a unit matrix with size $N^2 \times N^2$. $N^2 = N \times N$ is the sample size of the leads.

Solving Supplementary Eq. (4) gives the voltages V_n and the current I_α . The Hall resistance and the longitudinal resistance can then be defined as [1]:

$$R_H^\alpha = \frac{V_2 - V_6}{I_\alpha}, \quad R_L^\alpha = \frac{V_2 - V_3}{I_\alpha}. \quad (7)$$

Symmetrize the resistances: Since the leads are unaligned, to eliminate the influences of the sample's shape to the Hall responses, one has to symmetrize obtained results. In the standard processes with a magnetic field \mathbf{B} applied perpendicularly, the symmetrized Hall and longitudinal resistances satisfies $R_H = [R_H^\alpha(\mathbf{B}) - R_H^\alpha(-\mathbf{B})]/2$ and $R_L = [R_L^\alpha(\mathbf{B}) + R_L^\alpha(-\mathbf{B})]/2$ [1], respectively. Nevertheless, the magnetic field is absent for the considered models. Fortunately, the key point for $R_{H/L}^\alpha(\mathbf{B})$ and $R_{H/L}^\alpha(-\mathbf{B})$ is that they transpose the transmission-coefficient matrix in Supplementary Eq. (4).

Following a similar process, we suggest to adopt the complex conjugation of the hopping matrix along the α direction, where $\mathcal{T}_\alpha \rightarrow \mathcal{T}_\alpha^\dagger$. In this perspective, such a process also transposes the matrix in Supplementary Eq. (4). Similarly, one calculates the resistances along the α direction by adopting \mathcal{T}_α and $\mathcal{T}_\alpha^\dagger$. Then, the symmetrized Hall and longitudinal resistances are obtained through $R_H = [R_H^\alpha(\mathcal{T}_\alpha) - R_H^\alpha(\mathcal{T}_\alpha^\dagger)]/2$ and $R_L = [R_L^\alpha(\mathcal{T}_\alpha) + R_L^\alpha(\mathcal{T}_\alpha^\dagger)]/2$. For simplicity, in the main text and in the calculations below, such a process is simplified as

$$\begin{aligned} R_H &\equiv \frac{R_H^\alpha(\mathcal{T}_\alpha) - R_H^\alpha(\mathcal{T}_\alpha^\dagger)}{2} = \frac{V_2 - V_6}{I_\alpha} = \frac{V_2 - V_6}{I}, \\ R_L &\equiv \frac{R_L^\alpha(\mathcal{T}_\alpha) + R_L^\alpha(\mathcal{T}_\alpha^\dagger)}{2} = \frac{V_2 - V_3}{I_\alpha} = \frac{V_2 - V_3}{I}. \end{aligned} \quad (8)$$

Note 4: Effective model for the surface states

In this section, we present the details of the deviation of the effective model for the surface states. We start from the full Hamiltonian of the system in Eq.(3) in the main text and present the deviation of the effective low energy Hamiltonian on different surfaces separately. To proceed, we expand the Hamiltonian in Eq.(3) around the Γ point in the long wave limit, which has the form

$$\begin{aligned} \mathcal{H}(k_x, k_y, k_z) &= (2m_x\tau_z\sigma_z - \gamma\tau_0\sigma_z) - (m_x\tau_z\sigma_z k_x^2 + 2t_s\tau_0\sigma_x k_x) \\ &\quad - [m\tau_z\sigma_z k_y^2 - (2A\tau_y\sigma_z - 2t_s\tau_0\sigma_y)k_y] \\ &\quad - (m\tau_z\sigma_z k_z^2 - 2A\tau_x\sigma_z k_z). \end{aligned} \quad (9)$$

We first derive the effective Hamiltonian $\mathcal{H}^x(k_y, k_z)$. Using the $k \cdot p$ theory, the momentum k_x can be replaced by $-i\partial_x$, which recast the Hamiltonian Eq.(3) in the main text into

$$\begin{aligned} \mathcal{H}(x, k_y, k_z) &= (2m_z\tau_z\sigma_z - \gamma\tau_0\sigma_z) + (m_x\tau_z\sigma_z\partial_x^2 + 2it_s\tau_0\sigma_x\partial_x) \\ &\quad - [m\tau_z\sigma_z k_y^2 - (2A\tau_y\sigma_z - 2t_s\tau_0\sigma_y)k_y] \\ &\quad - (m\tau_z\sigma_z k_z^2 - 2A\tau_x\sigma_z k_z). \end{aligned} \quad (10)$$

We then separate this Hamiltonian into $\mathcal{H}(x, k_y, k_z) = \Delta\mathcal{H}(k_y, k_z) + \mathcal{H}_{\partial_x}(x)$, where

$$\begin{aligned}\Delta\mathcal{H}(k_y, k_z) &= (2m_x\tau_z\sigma_z - \gamma\tau_0\sigma_z) - [m\tau_z\sigma_z k_y^2 - (2A\tau_y\sigma_z - 2t_s\tau_0\sigma_y)k_y] - (m\tau_z\sigma_z k_z^2 - 2A\tau_x\sigma_z k_z), \\ \mathcal{H}_x(x) &= m_x\tau_z\sigma_z\partial_x^2 + 2it_s\tau_0\sigma_x\partial_x.\end{aligned}\tag{11}$$

Note that the eigenfunction (eigenenergy) for the full Hamiltonian \mathcal{H} can be expressed in terms of the direct product (summation) of the eigenfunctions (eigenenergies) of $\Delta\mathcal{H}(k_y, k_z)$. The Schrodinger equation of $\mathcal{H}_x(x)\psi(x)$ reads

$$[m_x\tau_z\sigma_z\partial_x^2 + 2it_s\tau_0\sigma_x\partial_x]\psi(x) = E\tau_0\sigma_0.\tag{12}$$

In the low-energy regime near the Γ point, the energy E can be approximately set to be 0. The above Schrodinger equation then becomes

$$[2it_s\tau_0\sigma_x]\partial_x\psi(x) = -m_z\tau_z\sigma_z\partial_x^2\psi(x).\tag{13}$$

Multiplying $\tau_0\sigma_x$ from the both sides yields

$$\tau_0\sigma_0\partial_x\psi(x) = \frac{m_z}{2t_s}\tau_z\sigma_y\partial_x^2\psi(x).\tag{14}$$

Note that we have used the relation $[\tau_0\sigma_x][\tau_z\sigma_z] = -i\tau_z\sigma_y$ in deriving this equation.

It is straightforward to notice that the solution to Supplementary Eq. (14) has the general form $\psi(x) = \chi e^{-\text{sgn}(x)\lambda x}$. Substituting this into Supplementary Eq. (14) and eliminating the common terms on both sides of the equation, we obtain

$$\tau_z\sigma_y\chi = \frac{-2\text{sgn}(x)t_s}{m_z\lambda}\chi.\tag{15}$$

Diagonalizing this eigenequation gives the relation $\lambda = \pm 2\text{sgn}(x)t_s/m_z$ as the eigenenergy of Supplementary Eq. (15) is $\eta = \pm 1$. If $t_s = 0$, we have $\lambda = 0$. In this case the wavefunction $\psi(x)$ is a constant independent of x , indicating the absence of the localized surface states. Since the wavefunction $\psi(x) \propto e^{-\text{sgn}(x)\lambda x}$ has to converge when $x \rightarrow \pm\infty$, the parameter λ has only one allowed value $\lambda = 2t_s/m_z$ as $t_s/m_z > 0$. We thus have the eigenenergy of Supplementary Eq. (15) is $\eta = -\text{sgn}(x)$ and two degenerated eigenstates are

$$\chi_1 = \frac{1}{\sqrt{2}} \begin{pmatrix} -i \\ \text{sgn}(x) \\ 0 \\ 0 \end{pmatrix}, \quad \chi_2 = \frac{1}{\sqrt{2}} \begin{pmatrix} 0 \\ 0 \\ i \\ \text{sgn}(x) \end{pmatrix}.\tag{16}$$

Consequently, the effective Hamiltonian can then be calculated by using [4]

$$\mathcal{H}^x(k_y, k_z) \propto \langle \chi_1, \chi_2 | \Delta H_{k_y, k_z} | \chi_1, \chi_2 \rangle \propto [-2Ak_z\sigma_x - 2Ak_y\sigma_y - \text{sgn}(x)2t_s k_y\sigma_z],\tag{17}$$

which further gives

$$\mathcal{H}^x(k_y, k_z) = \mathcal{B}_6 k_y \sigma_y + \text{sgn}(x) \mathcal{B}_7 k_y \sigma_z + \mathcal{B}_8 k_z \sigma_x.\tag{18}$$

Here, \mathcal{B}_6 , \mathcal{B}_7 and \mathcal{B}_8 are system parameters than can be determined by fitting the band structure with that obtained from the full Hamiltonian. Supplementary Eq. (18) shows that the gapless Dirac cone centers at the Γ point with $k_y = k_z = 0$. Therefore, the momentum surface locking is obviously absent on these two surfaces, in consistent with that in the main text.

The effective model Hamiltonian on the x - y plane can be derived in the same token. We replace k_z with $-i\partial_z$, which recasts Eq. (9) into $\mathcal{H}(k_x, k_y, z) = \Delta\mathcal{H}(k_x, k_y) + \mathcal{H}_z(z)$ with

$$\begin{aligned}\Delta\mathcal{H}(k_x, k_y) &= (2m_x\tau_z\sigma_z - \gamma\tau_0\sigma_z) - [m\tau_z\sigma_z k_y^2 - (2A\tau_y\sigma_z - 2t_s\tau_0\sigma_y)k_y] - (m_x\tau_z\sigma_z k_x^2 + 2t_s\tau_0\sigma_x k_x), \\ \mathcal{H}_z(z) &= m\tau_z\sigma_z\partial_z^2 - 2iA\tau_x\sigma_z\partial_z.\end{aligned}\tag{19}$$

The Schrodinger equation for $\mathcal{H}_z(z)$ in the limit of $E = 0$ is $m\tau_z\sigma_z\partial_z^2\psi(z) - 2iA\tau_x\sigma_z\partial_z\psi(z) \approx 0$, which, after substituting the typical solution in the form of $\psi(z) = \chi e^{-\text{sgn}(z)\lambda z}$, becomes

$$m\tau_y\sigma_0\lambda\chi = 2A\tau_0\sigma_0\text{sgn}(z)\chi.\tag{20}$$

Solving this eigenequation gives the eigenenergy $\eta = \text{sgn}(z)$ and corresponding eigenfunctions

$$\chi_1 = \frac{1}{\sqrt{2}} \begin{pmatrix} i \\ 0 \\ \text{sgn}(z) \\ 0 \end{pmatrix}, \quad \chi_2 = \frac{1}{\sqrt{2}} \begin{pmatrix} 0 \\ i \\ 0 \\ \text{sgn}(z) \end{pmatrix}.\tag{21}$$

The effective low-energy Hamiltonian on this plane is thus

$$\begin{aligned}\mathcal{H}^z(k_x, k_y) &= \langle \chi_1, \chi_2 | \Delta H(k_x, k_y) | \chi_1, \chi_2 \rangle \\ &= \text{sgn}(z) \{ [\mathcal{B}_1 k_y - \text{sgn}(z)\kappa] \sigma_z + \mathcal{B}_2 k_y \sigma_y + \mathcal{B}_3 k_x \sigma_x \},\end{aligned}\tag{22}$$

where $\mathcal{B}_{1,2,3}$ and $\kappa \propto \gamma$ are system parameters. Supplementary Eq. (22) shows that, in the absence of $\mathcal{B}_2 k_y \sigma_y$ term, the surface bands are gapless Dirac cones located at $k_x = 0$ and $k_y = \text{sgn}(x)\kappa/\mathcal{B}_1$. Because $\text{sgn}(z)$ takes opposite values on opposite surfaces, this reveals that the surface Dirac cones are also oppositely shifted along k_y direction. Moreover, the $\mathcal{B}_2 k_y \sigma_y$ term opens band gaps into those surface states, giving rise to the half quantized Chern number on each surface.

On the x - z plane, the full Hamiltonian $\mathcal{H}(k_x, k_z, y) = \Delta\mathcal{H}(k_x, k_z) + H_y(y)$ with

$$\begin{aligned}\Delta\mathcal{H}(k_x, k_z) &= (2m_x\tau_z\sigma_z - \gamma\tau_0\sigma_z) + (-m\tau_z\sigma_z k_z^2 + 2A\tau_x\sigma_z k_z) - (m_x\tau_z\sigma_z k_x^2 + 2t_s\tau_0\sigma_x k_x), \\ \mathcal{H}_{\partial_y}(y) &= m\tau_z\sigma_z\partial_y^2 - 2iA\tau_y\sigma_z\partial_y + 2it_s\tau_0\sigma_y\partial_y \approx m\tau_z\sigma_z\partial_y^2 - 2iA\tau_y\sigma_z\partial_y,\end{aligned}\tag{23}$$

where the $2it_s\tau_0\sigma_y\partial_y$ term is disregarded in the second equation since the spin-orbit coupling t_s is considerably weaker than the onsite energy m and A . Using the relation $[\tau_y\sigma_z][\tau_z\sigma_z] = i\tau_x\sigma_0$ and substituting the typical solution with form $\psi(y) = \chi e^{-\text{sgn}(y)\lambda y}$ into the Schrodinger equation for $\mathcal{H}_{\partial_y}(y)$, we arrive at

$$m\tau_x\sigma_0\lambda\chi = -2A\text{sgn}(y)\chi.\tag{24}$$

Solving this eigenequation further gives $\eta = -\text{sgn}(y)$ and

$$\chi_1 = \frac{1}{\sqrt{2}} \begin{pmatrix} 1 \\ 0 \\ \text{sgn}(y) \\ 0 \end{pmatrix}, \quad \chi_2 = \frac{1}{\sqrt{2}} \begin{pmatrix} 0 \\ 1 \\ 0 \\ \text{sgn}(y) \end{pmatrix}, \quad (25)$$

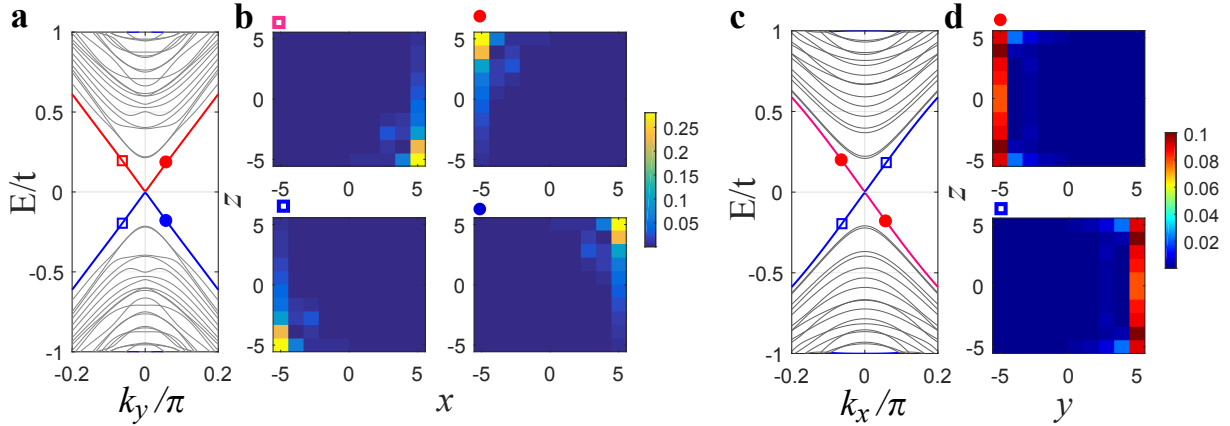
Then we can finally calculate the effective low-energy Hamiltonian

$$\mathcal{H}^y(k_x, k_z) = \langle \chi_1, \chi_2 | \Delta H(k_x, k_z) | \chi_1, \chi_2 \rangle = \text{sgn}(y) \{ [\mathcal{B}_4 k_z - \text{sgn}(y) \kappa] \sigma_z + \mathcal{B}_5 k_x \sigma_x \}. \quad (26)$$

This equation evidently shows that the surface bands are gapless Dirac cones located oppositely at $k_x = \text{sgn}(y) \kappa / \mathcal{B}_4$ and $k_z = 0$ on opposite surfaces, exhibiting a momentum surface locking.

Note 5: Chiral boundary states with quantized Chern number on x - y plane

A. Numerical results: wave function distributions



Supplementary Fig. 7: Boundary states inherent to the quantized Chern number.

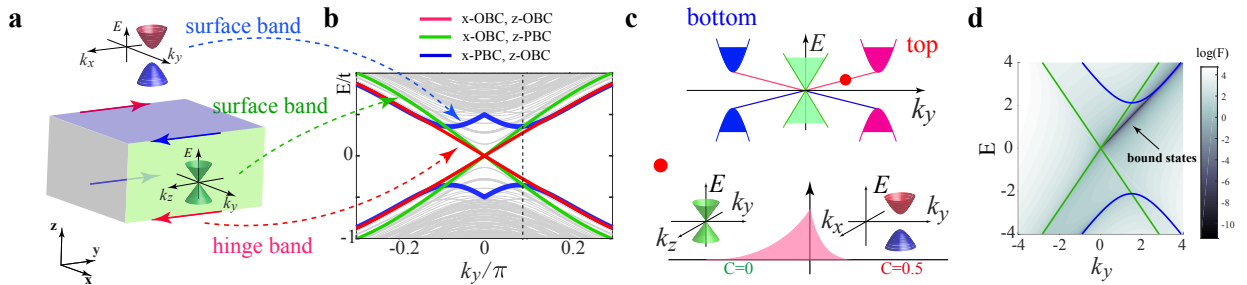
a Band structure as a function of k_y for a ribbon geometry with open boundary conditions along x and z directions. The gray lines refer to the high energy surface bands while the red and blue lines are gapless boundary bands. The squares and circles mark four representative boundary states, whose wavefunction distributions across the x - z plane are displayed correspondingly in **b**. **c** Band structure versus k_x for a ribbon geometry with open boundary conditions along y and z directions. The wavefunction distributions for the boundary states represented by blue and red markers are shown in **d**. Here, the sample sizes along the open boundary directions are $N \times N = 10 \times 10$.

To clarify the edge picture of the chiral boundary states in scheme 1, we examine the wavefunction distributions for the boundary states represented by the colorful markers in

Supplementary Figs. 7a and c. In a ribbon geometry extending infinitely along y direction while terminating along x and z directions, the results plotted in Supplementary Fig. 7b shows that the wave function distributions for four representative boundary states marked in a are all fully confined to the hinges. Interestingly, when the Fermi energy $E_f < 0$ the two boundary states represented by blue markers are confined to one pair of diagonal hinges while the two boundary states represented by red markers at $E_f > 0$ are confined to the other pair of diagonal hinges. Consequently, the location of these hinge states can be manipulated by tuning the Fermi energy. In contrast, In a ribbon geometry extending infinitely along x direction, the boundary states are wide extended across the entire z direction as shown in Supplementary Fig. 7d, and their locations as well as the chirality are independent of the Fermi energy E_f .

B. Half-integer-Chern-number-difference induced bound states

The bulk-boundary correspondence states that edge states exist at the domain connecting two regions with different integer topological invariants and that the number of these edge states is identical to the variation of the topological invariants across this domain. In 3D QAHE proposed in the main text, the Chern numbers across a hinge between top (bottom) and front (back) surfaces are $\mathcal{C} = 0.5$ and $\mathcal{C} = 0$, respectively, violating the conventional bulk-boundary correspondence. However, we show that a localized chiral hinge state still exists in this case.



Supplementary Fig. 8: Hinge states. **a** Schematic plot for the chiral hinge states along y direction. The band structures for the top surface and the front surface are also displayed. **b** Band structure for a ribbon geometry extending infinitely along y direction while finite along x and z directions under different boundary conditions. The gray lines refer to the surface bands whereas the red, green, and blue lines represent the boundary bands under x -OBC z -OBC, x -OBC z -PBC, and x -PBC z -OBC, respectively. **c** A cartoon for the band structure of the ribbon along k_y direction is shown in the top panel. The red circle marks an representative boundary state, whose wavefunction distribution across the hinge between top and front surfaces are plotted in the bottom panel. **d** $\log[\mathcal{F}]$ as a function of k_y . The green and blue bands are the gapless band for the front surface and the gap band for the top surface. The thick gray line refers to the chiral hinge state.

As shown in Supplementary Fig. 8b, under x -OBC while z -PBC, the top and bottom surface states are eliminated by the periodic boundary condition along z direction. We find a

gapless Dirac cone centered at $k_y = 0$. Under x -PBC while z -OBC, the front and back surface states are eliminated and we thus find two gaped Dirac cone centered at opposite k_y . This can be ascribed to the momentum-surface locking, which shifts the top and bottom surface states oppositely. Importantly, under x -OBC and z -OBC, we find an unexpected boundary band (red lines) connecting the two neighboring surface states and thus is located on the hinge between them. As depicted in the top panel in Supplementary Fig. 8c, any boundary state on this band at finite momentum locates at the direction gap of both front band and top band. Corresponding wavefunction for this boundary state must decay exponentially into both surface as shown in the bottom panel of Supplementary Fig. 8c, resulting in a confined hinge state.

To further confirm this hinge state, we present an analytical study based on the effective Hamiltonian obtained in Sec.V. We start from the following Hamiltonian

$$\begin{aligned}\mathcal{H}^x(k_y, k_z) &= \mathcal{B}_6 k_y \sigma_y + \text{sgn}(x) \mathcal{B}_7 k_y \sigma_z + \mathcal{B}_8 k_z \sigma_x, \\ \mathcal{H}^z(k_x, k_y) &= \text{sgn}(z) \{ [\mathcal{B}_1 k_y - \text{sgn}(z) \kappa] \sigma_z + \mathcal{B}_2 k_y \sigma_y + \mathcal{B}_3 k_x \sigma_x \}.\end{aligned}\quad (27)$$

Without of lose generality, we take $\mathcal{B}_1 = \mathcal{B}_2 = \mathcal{B}_3 = 1$, $\mathcal{B}_6 = \mathcal{B}_8 = 1$, $\mathcal{B}_7 = -1$, $x < 0$, $z > 0$ to obtain a qualitative picture for the hinge state. Then, the above Hamiltonian can be simplified into

$$\begin{aligned}\mathcal{H}^x(k_y, k_z) &= [k_z \sigma_x + (\sigma_y + \sigma_z) k_y], \\ \mathcal{H}^z(k_x, k_y) &= [k_y - \kappa] \sigma_z + k_y \sigma_y + k_x \sigma_x.\end{aligned}\quad (28)$$

Specifically, the gaped and gapless Hamiltonian possess Chern number $\mathcal{C} = 0.5$ and $\mathcal{C} = 0$, respectively. Hereinbelow, we prove that the half-integer Chern number difference can also lead to the bound states.

For the hinge along y direction, k_z should be connected with k_x [$k_x \equiv k_z$], and the above Hamiltonian can be modified as:

$$\begin{aligned}\mathcal{H}_1 &= [k_z \sigma_x + (\sigma_y + \sigma_z) k_y], \\ \mathcal{H}_2 &= [k_y - \kappa] \sigma_z + k_y \sigma_y + k_z \sigma_x.\end{aligned}\quad (29)$$

The above Hamiltonian describe the domain in Supplementary Fig. 8c. Replacing $k_z \rightarrow -i\partial_z$ yields

$$\begin{aligned}\mathcal{H}_1 &= [-i\partial_z \sigma_x + (\sigma_y + \sigma_z) k_y] \quad \text{if } z > 0, \\ \mathcal{H}_2 &= [k_y - \kappa] \sigma_z + k_y \sigma_y - i\partial_z \sigma_x \quad \text{if } z < 0.\end{aligned}\quad (30)$$

As these both \mathcal{H}_1 and \mathcal{H}_2 contain only the first order derivative of z , the solutions to their eigenequations can be typically expressed as $\Psi^1 = [\psi_1^1, \psi_2^1] e^{\lambda_1 z}$ and $\Psi^2 = [\psi_1^2, \psi_2^2] e^{\lambda_2 z}$. We then arrive at [4]

$$\begin{aligned}\mathcal{H}_1 \Psi^1 &= [-i\partial_z \sigma_x + (\sigma_y + \sigma_z) k_y] \Psi^1 = E \Psi^1 \quad \text{if } z > 0, \\ \mathcal{H}_2 \Psi^2 &= \{-i\partial_z \sigma_x + [k_y - \kappa] \sigma_z + k_y \sigma_y\} \Psi^2 = E \Psi^2 \quad \text{if } z < 0.\end{aligned}\quad (31)$$

The above Hamiltonian can be further rewritten as

$$\begin{aligned}| -E - i\lambda_1 \sigma_x + k_y \sigma_z + k_y \sigma_y | &= 0 \quad \text{if } z > 0, \\ | -E - i\lambda_2 \sigma_x + [k_y - \kappa] \sigma_z + k_y \sigma_y | &= 0 \quad \text{if } z < 0.\end{aligned}\quad (32)$$

(i) When $z > 0$, we find the following relations

$$|-E - i\lambda_1\sigma_x + k_y\sigma_z + k_y\sigma_y| = \det \begin{pmatrix} -E + k_y & -i\lambda_1 - ik_y \\ -i\lambda_1 + ik_y & -E - k_y \end{pmatrix} = E^2 - k_y^2 - (-\lambda_1^2 + k_y^2) = 0, \quad (33)$$

which gives $\lambda_1^\pm = \pm\sqrt{2k_y^2 - E^2}$. Since the wave function have to converge when $z \rightarrow +\infty$, this λ_1 has only one physically allowed value $\lambda_1 = \lambda_1^- = -\sqrt{2k_y^2 - E^2}$. Thus, the eigenstate is $\Psi^1 = [\psi_1^1, \psi_2^1]e^{\lambda_1^- x}$.

(ii) When $z < 0$, the following equation holds

$$|-E - i\lambda_2\sigma_x + [k_y - \kappa]\sigma_z + k_y\sigma_y| = \det \begin{pmatrix} -E + (k_y - \kappa) & -i\lambda_2 - ik_y \\ -i\lambda_2 + ik_y & -E - (k_y - \kappa) \end{pmatrix} = E^2 - (k_y - \kappa)^2 - (-\lambda_2^2 + k_y^2) = 0, \quad (34)$$

which gives the equation $\lambda_2^\pm = \pm\sqrt{k_y^2 + (k_y - \kappa)^2 - E^2}$. λ_2 has to be positive to ensure the convergence. Therefore, the eigenstate is $\Psi^2 = [\psi_1^2, \psi_2^2]e^{\lambda_2^+ z}$.

Substituting there two eigenstates into Supplementary Eq. 31, we then obtain

$$\begin{pmatrix} -E + k_y & -i\lambda_1^- - ik_y \\ -i\lambda_1^- + ik_y & -E - k_y \end{pmatrix} \begin{pmatrix} \psi_1^1 \\ \psi_2^1 \end{pmatrix} = 0, \\ \begin{pmatrix} -E + (k_y - \kappa) & -i\lambda_2^+ - ik_y \\ -i\lambda_2^+ + ik_y & -E - (k_y - \kappa) \end{pmatrix} \begin{pmatrix} \psi_1^2 \\ \psi_2^2 \end{pmatrix} = 0. \quad (35)$$

Thus

$$\psi_1^1 = -\frac{-i\lambda_1^- - ik_y}{-E + k_y}\psi_2^1, \\ \psi_1^2 = -\frac{-i\lambda_2^+ - ik_y}{-E + (k_y - \kappa)}\psi_2^2. \quad (36)$$

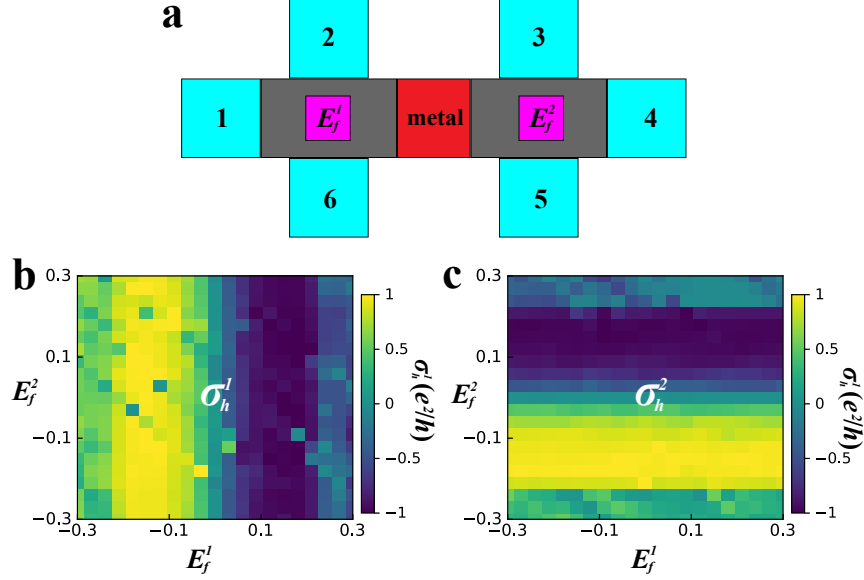
Moreover, the continuity condition for the wavefunctions at $z = 0$ ($\Psi^1|_{z=0} = \Psi^2|_{z=0}$) give another equation

$$-\frac{-i\lambda_1^- - ik_y}{-E + k_y} + \frac{-i\lambda_2^+ - ik_y}{-E + (k_y - \kappa)} = 0, \quad (37)$$

where $\lambda_1^- = -\sqrt{2k_y^2 - E^2}$ and $\lambda_2^+ = \sqrt{k_y^2 + (k_y - \kappa)^2 - E^2}$. This continuity equation can be equivalently expressed as

$$\mathcal{F} = |(-i\lambda_1^- - ik_y)[-E + (k_y - \kappa)] - (-i\lambda_2^+ - ik_y)(-E + k_y)| = 0. \quad (38)$$

Solving this continuity equation can finally give the boundary states shown in Supplementary Fig. 8d. The existence of solutions to Supplementary Eq. 38 also demonstrates the existence of boundary states between top surface with Chern number $\mathcal{C} = 0.5$ and front surface with Chern number $\mathcal{C} = 0$. Besides, this boundary state is well confined to the hinge as the wave functions $\Psi^{1,2}$ decay exponentially along z direction. Similar processes can be applied to the system along other directions.



Supplementary Fig. 9: In-memory computing. **a** Schematic for a setup with two unit cells connecting in series. 1-6 are six metallic leads. Gray regions denotes the 3D QAHE systems. the red region refers to a metal connecting two unit cell in series. The magenta regions represent the top gate for each unit cell. **b,c** Hall conductances σ_h^1 and σ_h^2 on the E_f^1 - E_f^2 plane.

Note 6: Multiple unit-cell for in-memory computing

As shown in Supplementary Fig. 9a, in a system with two 3D QAHE systems connecting in series through a metal, the transport properties can also be unveiled through the Landauer-Büttiker theory. Specifically, since the Fermi energies E_f^1 and E_f^2 for two unit cell can be manipulated independently through the top gates, we calculate the Hall conductances $\sigma_h^1 = (V_2 - V_6)/I$ and $\sigma_h^2 = (V_3 - V_5)/I$, and display the results in Supplementary Figs. 9b and c, respectively. It shows that the Hall conductance σ_h^1 (σ_h^2) for the first (second) unit cell switches from $-e^2/h$ to e^2/h when tuning the Fermi energy across the charge neutral point, in consistent with the results in the main text. Most importantly, σ_h^1 (σ_h^2) only depends on E_f^1 (E_f^2), which thus demonstrates that these two unit cells can be operated independently during the computational process.

Supplementary References

1. S. Datta, *Electronic Transport in Mesoscopic Systems*, Cambridge University Press, Cambridge, England, (1995).
2. D. J. Thouless, M. Kohmoto, M. P. Nightingale, and M. den Nijs, Quantized Hall Conductance in a Two-Dimensional Periodic Potential, *Phys. Rev. Lett.* **49**, 405 (1982).
3. Z. Q. Zhang, B. L. Wu, J. T. Song, and H. Jiang, Topological Anderson insulator in

- electric circuits, *Phys. Rev. B* **100**, 184202 (2019).
4. S. Q. Shen, Topological insulators, Berlin, Springer (2012).
 5. P. W. Anderson, Absence of diffusion in certain random lattices, *Phys. Rev.* **109**, 1492 (1958).